





Topological phase transitions of non-Abelian charged nodal lines in spring-mass systemsHaedong Park ¹, Stephan Wong ¹, Adrien Bouhon², Robert-Jan Slager ², and Sang Soon Oh ^{1,*}¹*School of Physics and Astronomy, Cardiff University, Cardiff CF24 3AA, United Kingdom*²*TCM Group, Cavendish Laboratory, University of Cambridge, Cambridge CB3 0HE, United Kingdom*

(Received 2 April 2022; revised 1 June 2022; accepted 3 June 2022; published 16 June 2022)

Although a large class of topological materials has uniformly been identified using symmetry properties of wave functions, the past two years have seen the rise of multigap topologies beyond this paradigm. Given recent reports of unexplored features of such phases, platforms that are readily implementable to realize them are therefore desirable. Here we demonstrate that multigap topological phase transitions of non-Abelian charged nodal lines arise in classical phonon waves. By adopting a simple spring-mass system, we construct nodal lines of a three-band system. The braiding process of the nodal lines is readily performed by adjusting the spring constants. The generation and annihilation of the nodal lines are then analyzed using the Euler class. Finally, we retrieve topological transitions from trivial nodal lines to a nodal link. Our work provides a simple platform that can offer diverse insights to not only theoretical but also experimental studies on multigap topology.

DOI: [10.1103/PhysRevB.105.214108](https://doi.org/10.1103/PhysRevB.105.214108)**I. INTRODUCTION**

The uncovering of topological insulators has opened an active field of physics [1,2], and the past decades have seen rapid progress on these effective topological phases. Topological classifications have in particular profited from the interplay with space-group symmetries [3–20]. Beyond these works on single-gap topologies, recent studies on the multigap conditions are, however, steadily rising [21,22]. The crux of these developments is the insight that degeneracies in a multigap system may carry non-Abelian charges [23–25] and that braiding a degeneracy around another in a different gap can hence render a system with similarly valued charges between two bands [23,24,26–28]. Such braiding and stability/instability of band degeneracies can then be described using Euler class [24,25,27–30], an integer-valued multigap topological invariant that is calculated over the Brillouin zone or a patch thereof in momentum space. That is, a nonzero integer-valued Euler class indicates that the band touchings in the patch are topologically obstructed to annihilate. Multigap topologies have been predicted to culminate in new effects such as specific monopole-antimonopole generation [30] that was recently observed in trapped ion experiments [31], as well as signatures in structural phase transitions [32,33], strained and magnetic electronic systems [24,34], and phononic systems [27,28,35–37].

Given these new features of non-Abelian charged degeneracies and multigap topological physics, a simple, intuitive, and easily tuneable but experimentally viable system is of interest. A highlight candidate in this regard is classical spring-mass systems [38–45]. Especially because if a spring-mass system is constituted in three-dimensional real space, it

may exhibit nodal line degeneracies that can have an intricate interplay with non-Abelian charges [22,26]. A nodal line is a set of degeneracies in a one-dimensional curved shape formed in three-dimensional momentum space [46]. Various types of nodal lines, e.g., nodal rings [47,48], nodal chains [49–54], nodal links [51–60], and nodal knots [58,59,61], have already been reported using metals [23,49,57], semimetals [51,52,56,59,61,62], electrical circuits [58], photonic media [48,50,54,55,63–65], and phononic crystals [36,47,60,66,67]. In addition, the non-Abelian multigap charges, or frame rotation charges [23,24,27,28], in three-band systems are especially insightful and amount to quaternion numbers. Consequently, if a simple phononic crystal having three bands exhibits nodal lines, it acts as a good platform to observe quaternion charges.

Here we predict phase transitions of multigap nodal lines quantified by Euler class using a class of simple and easily realizable spring-mass systems. The non-Abelian charged nodal lines are realized using phonon waves in a classical spring-mass system [38–45,68–74]. A unit cell of our system consists of only one mass and several springs, and the system's mechanical behavior is thus described by classical mechanical equations of motion. Some springs concerning on-site potentials [42–45,72–74] eliminate the degeneracy at the Γ point and enable a three-band nodal link. This heuristically amounts to removing the Nambu-Goldstone zero modes [37] by having different on-site potential. By braiding one nodal line around the other, we propose the principle of generating a nodal link from a trivial state featuring nodal rings. The phase transition is realized using the braiding process carried out by tuning the spring constants. Subsequently, we apply Euler class to characterize whether the nodal lines are topologically stable or can be annihilated pairwise. We finally also discuss the possible states and transitions of the nodal lines from the Euler-class viewpoint.

*ohs2@cardiff.ac.uk

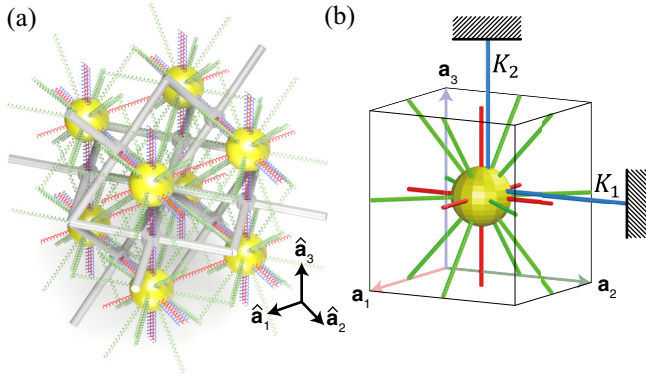


FIG. 1. A spring-mass phononic crystal. (a) Illustration of the spring-mass system in an orthorhombic lattice system. The yellow spheres have the mass m . The red and green are intersite springs that connect the first and second nearest neighbors, respectively. Each blue spring for the on-site potential connects a sphere (mass) and the fixed support, the gray structure. The red and blue springs are set to be parallel to each other along \mathbf{a}_2 and \mathbf{a}_3 directions. The intersite springs pass through the holes of the support, while the on-site springs are attached to the support. (b) The unit cell of (a) considered in Eq. (1).

II. SPRING-MASS SYSTEM

We consider the spring-mass system in a simple orthorhombic lattice, where the unit cell consists of a single mass and eleven springs, as shown in Fig. 1. We assume that all masses of the springs are ignored and only the sphere's mass m is considered. Spring constants concerning intersite energies are denoted by C_{ij} , where the subscripts i and j mean the connection directions. A spring whose spring constant is denoted by C_{ii} connects the first-nearest-neighbor masses along \mathbf{a}_i direction, where \mathbf{a}_i ($i = 1, 2, 3$) is the lattice vector. Springs with C_{ij} ($i \neq j$) connect the second-nearest-neighbor masses along the $\mathbf{a}_i \pm \mathbf{a}_j$ direction. We also consider two springs for the on-site potentials, and their spring constants are denoted by K_1 and K_2 [see Fig. 1(b)]. While phononic crystals generally exhibit the triple-point degeneracy at the Γ point, these anisotropic on-site springs lift the degeneracy.

A unit cell in the three-dimensional array is denoted by integer-valued $[h_1, h_2, h_3]$, where all subscripts correspond to \mathbf{a}_1 , \mathbf{a}_2 , and \mathbf{a}_3 directions, respectively. The equation of motion for the displacement $\mathbf{u}_{h_1, h_2, h_3}$ of a mass in the unit cell $[h_1, h_2, h_3]$ is given by $m\ddot{\mathbf{u}}_{h_1, h_2, h_3} = \sum_n \mathbf{f}_n$, where the right-hand term is the summation of the spring force \mathbf{f}_n exerted on the mass. The displacement vector can be expressed as $\mathbf{u}_{h_1, h_2, h_3}(\mathbf{x}, t) = \mathbf{u}_k e^{i\mathbf{k}\cdot\mathbf{x}} e^{-i\omega t} = \mathbf{u}_k e^{i\mathbf{k}\cdot(h_1\mathbf{a}_1 + h_2\mathbf{a}_2 + h_3\mathbf{a}_3)} e^{-i\omega t}$. Substituting this into the equation of motion leads to the following eigenvalue problem:

$$\frac{2}{m} \left[\sum_{i=1}^3 H_{ii} + \sum_{i,j} H_{ij} + \frac{1}{2} \sum_l K_l (\hat{\mathbf{d}}_l \otimes \hat{\mathbf{d}}_l) \right] \mathbf{u}_k = (\omega_k)^2 \mathbf{u}_k, \quad (1)$$

where $H_{ii} = C_{ii} \{1 - \cos(\mathbf{k} \cdot \mathbf{a}_i)\} \hat{\mathbf{a}}_i \otimes \hat{\mathbf{a}}_i$ and $H_{ij} = C_{ij} \{1 - \cos(\mathbf{k} \cdot \mathbf{a}_i + \mathbf{k} \cdot \mathbf{a}_j)\} \hat{\mathbf{a}}_{ij} \otimes \hat{\mathbf{a}}_{ij}$ are the Hamiltonians for the intersite interactions along the \mathbf{a}_i and $\mathbf{a}_i \pm \mathbf{a}_j$ directions, respectively. $\hat{\mathbf{a}}_i$, $\hat{\mathbf{a}}_{ij}$, and $\hat{\mathbf{a}}_{i\bar{j}}$ are the unit vectors along \mathbf{a}_i , $\mathbf{a}_i + \mathbf{a}_j$,

and $\mathbf{a}_i - \mathbf{a}_j$, respectively. In H_{ij} ($ij = 12, 23, 31, 1\bar{2}, 2\bar{3}, 3\bar{1}$), if the subscript j is $\bar{1}, \bar{2}$, or $\bar{3}$, then $\mathbf{k} \cdot \mathbf{a}_j$ is replaced with $-\mathbf{k} \cdot \mathbf{a}_j$. The last term entails the on-site potential, and $\hat{\mathbf{d}}_l = \mathbf{d}_l / |\mathbf{d}_l|$ is the unit vector along the on-site spring connection. The detailed derivations are in Appendix A. Although Fig. 1 shows an orthorhombic unit cell and the intersite interactions in Eq. (1) are only along the first and second nearest neighbors, we can also consider unit cells in the other lattice systems and the interactions between the third nearest neighbors. Appendixes A and B also cover these general cases.

III. BRAIDING OF NON-ABELIAN CHARGED NODAL LINES

The real-valued 3×3 Hamiltonian in Eq. (1) is symmetric and positive definite for any wave vector \mathbf{k} . Thus the three eigenstates \mathbf{u}_k^1 , \mathbf{u}_k^2 , and \mathbf{u}_k^3 form an $\text{SO}(3)$ orthonormal frame. Unless the degeneracies form an accidental triple point [27,75], as enforced, e.g., by the Goldstone modes [36,37], the generically stable band crossings in \mathcal{PT} -symmetric systems are nodal lines [76] formed by only two adjacent bands. The non-Abelian frame charge for a nodal line is determined by which bands are connected by the nodal line and which band is gapped [23,24,26–28,37]. A closed loop that encloses a nodal line is considered. Along this loop one obtains the resulting frame charge by keeping track of the rotation of the orthonormal frame $\{\mathbf{u}_k^n\}_{n=1}^3$ via parallel transport. The nodal lines of a three-band system turn out to be characterized by the elements of the quaternion group $\mathbb{Q} = \{\pm i, \pm j, \pm k, -1, +1\}$ [23,24]. The frame charge contains the information about which bands form a nodal line in a multigap system. For example, the frame charge of the nodal line formed by the first and second (by the second and third) bands can be denoted as $\pm k$ ($\pm i$), as shown in Fig. 2(a). The detailed explanations are in Appendix C. The closed loop can also be set to encircle two or more nodal lines. Its frame charge is expressed as the multiplication of the frame charges of each nodal line, and it satisfies the anticommutation relations of the quaternion charges.

Topological phase transitions can be achieved through braiding of the frame charges, which flips their signs due to their non-Abelian nature [23,24,26–28]. As mentioned in the above, a closed loop can encircle two nodal lines. If the two nodal lines are equivalently (oppositely) charged, the frame charge is -1 ($+1$), meaning that they carry a nontrivial (trivial) charge [23,24]. The resultant frame charge can vary depending on the choice of the path [24]. Let us consider a closed loop C that encircles both nodal lines L_1 and L_2 and does not pass nodal rings R_1 and R_2 in Fig. 2(b). Here we assume that the frame charge calculated along this loop is -1 , and thereby the frame charges of L_1 and L_2 are the same. We braid P_1 and P_2 in Fig. 2(b) around Q_1 and Q_2 , respectively; they move under L_1 [see Fig. 2(c)], then over L_1 [see Fig. 2(d)]. In Fig. 2(d), if the closed loop C passes through R_1 (or R_2), the frame charge becomes $+1$. The same explanation can be applied to the nodal rings R_1 and R_2 in Figs. 2(b)–2(d). In other words, after completing the braiding process of P_1 and P_2 around the Q_1 and Q_2 , respectively, all their signs are flipped [see Fig. 2(d)]. Because the frame charges of Q_1 and Q_3 (and Q_2 and Q_4) are trivial in Fig. 2(d), they can be

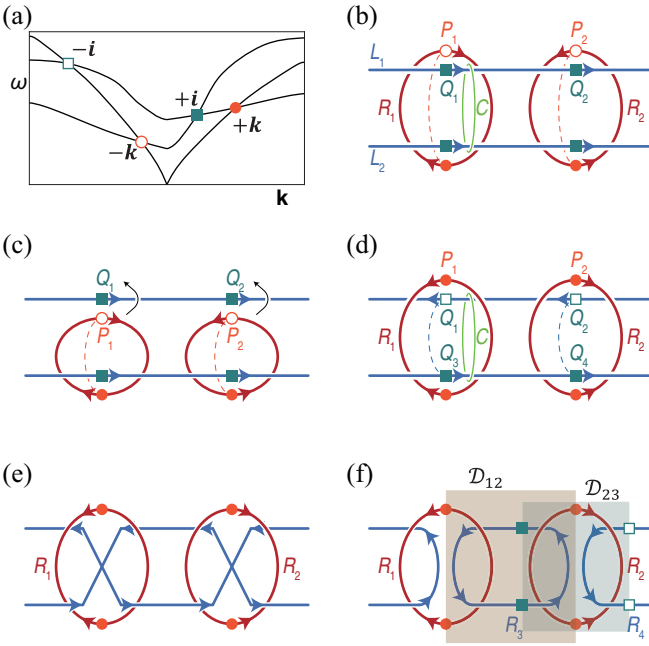


FIG. 2. Schematics of braiding nodal lines. (a) Frame charges of the nodal lines in a three-band system. The open and filled symbols indicate opposite charges, and the circles and rectangles mean $\pm k$ and $\pm i$, respectively. (b)–(d) Braiding of P_1 and P_2 around Q_1 and Q_2 , respectively. After braiding, all these four points change their signs. The dotted curves are the Dirac strings where $[\mathbf{u}_k^1, \mathbf{u}_k^2]$ (b)–(c) and $[\mathbf{u}_k^2, \mathbf{u}_k^3]$ (d) flip their signs. (e) Phase transition between (d) and (f). Q_1 and Q_3 that were in opposite frame charges in (d) are now annihilated. Q_2 and Q_4 do the same. (f) Final formation of the nodal link. The closed surfaces enclosing the rings R_3 and R_2 are denoted as \mathcal{D}_{12} and \mathcal{D}_{23} , respectively. In (b)–(f), red and blue arrows on the nodal lines indicate their orientations deduced from their frame charges.

annihilated pairwise, as shown in Fig. 2(e). Finally, they reach the nodal link in Fig. 2(f).

The stability of the nodal lines in the nodal link can be characterized by the Euler class calculated on the closed patch which nodal lines pass through [22,24]. If the Euler class is zero (nonzero), the nodal lines in the patch are unstable (stable) [24]. The surfaces \mathcal{D}_{12} and \mathcal{D}_{23} in Fig. 2(f) enclose R_3 and R_2 , respectively. In other words, through \mathcal{D}_{12} , only nodal lines of R_1 and R_2 exit, and no other lines pierce \mathcal{D}_{12} . Likewise, through \mathcal{D}_{23} only the nodal lines of R_3 and R_4 pass. If we observe the outward orientations at all four nodes where R_1 or R_2 touch \mathcal{D}_{12} , as marked in Fig. 2(f), we infer that the nodal lines of R_1 and R_2 are stable due to the nonzero Euler class. On the other hand, the patch \mathcal{D}_{23} has both inward and outward nodal lines. Thus we expect the zero-valued Euler class and unstable R_3 and R_4 . This means that R_3 and R_4 can be reversely transformed toward Figs. 2(e) and 2(d).

IV. PHASE TRANSITIONS IN SPRING-MASS SYSTEM

The phase transition from trivial nodal lines to a nodal link can be realized in our spring-mass system. Equation (1) receives the lattice vectors and spring constants as input parameters and outputs the eigenfrequencies ω_k^n and eigenstates \mathbf{u}_k^n , where the superscript n is the band

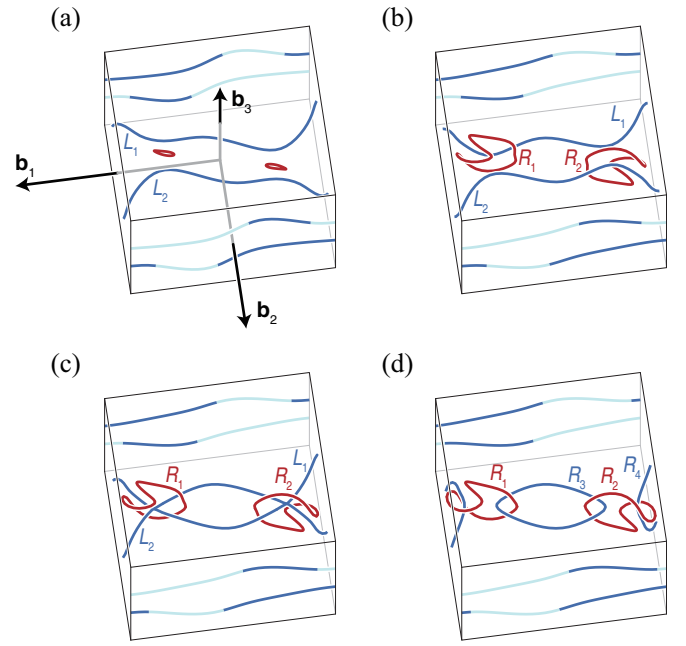


FIG. 3. Evolution of nodal lines. The red and blue nodal lines are degeneracies by $\omega_k^2 - \omega_k^1$ and $\omega_k^3 - \omega_k^2$, respectively. (a) Trivial state with $\Delta C_{12} = 42$ and $\Delta C_{31} = 15$. (b) Braided state after tuning ΔC_{12} to 20. (c) Phase transition by ΔC_{31} to 10.06. Degeneracies by $\omega_k^3 - \omega_k^2$ temporarily exhibit a nodal chain. (d) Nodal link by ΔC_{31} to 5. The parameters for the nodal link in (d) is listed in Table I of Appendix B.

number ($n = 1, 2, 3$). We use the values listed in Table I of Appendix B, except for C_{12} , $C_{1\bar{2}}$, C_{31} , and $C_{3\bar{1}}$. If we write $C_{12} = C_{12}^0 + \Delta C_{12}$, $C_{1\bar{2}} = C_{12}^0 - \Delta C_{12}$, $C_{31} = C_{31}^0 + \Delta C_{31}$, and $C_{3\bar{1}} = C_{31}^0 - \Delta C_{31}$ (where $C_{12}^0 = 75$ and $C_{31}^0 = 35$), the four spring constants can be controlled by tuning only ΔC_{12} and ΔC_{31} . The degeneracies by $\omega_k^2 - \omega_k^1$ and $\omega_k^3 - \omega_k^2$ are plotted as red and blue nodal lines, respectively, in Fig. 3. Note that all the nodal lines are inversion symmetric about the Γ point because Eq. (1) is \mathcal{T} symmetric and \mathcal{P} symmetric. We start with the trivial nodal lines [see Fig. 3(a)] by selecting $\Delta C_{12} = 42$ and $\Delta C_{31} = 15$. The nodal lines L_1 and L_2 in Fig. 3(a) have the same orientations directing the same boundary if the closed loop is placed like Fig. 2(b). We change ΔC_{12} to 20, then the rings R_1 and R_2 become bigger, as shown in Fig. 3(b). The frame charges of L_1 and L_2 are now opposite if the closed loop's path is set like Fig. 2(d). This configuration enables the pairwise annihilation of L_1 and L_2 through the nodal rings R_1 and R_2 , as shown in Fig. 3(c), by decreasing ΔC_{31} to 10.06. Further decreasing ΔC_{31} to 5 makes the final nodal link in Fig. 3(d). The frame charge analyses for the situations in Fig. 3 are in Appendix C.

V. STABILITY AND INSTABILITY OF NODAL LINES

The Euler class [24,25,27,28,30] quantifies the pairwise annihilation and stability of the nodal lines' transition in Fig. 3. We focus the discussions on the nodal link in Fig. 3(d). Let us imagine a cube that encloses R_3 and denote its surface as \mathcal{D}_{12} [refer Fig. 2(f)]. This \mathcal{D}_{12} surface is pierced only by R_1 and R_2 , the degeneracies by $\omega_k^1 - \omega_k^2$. The Euler class χ

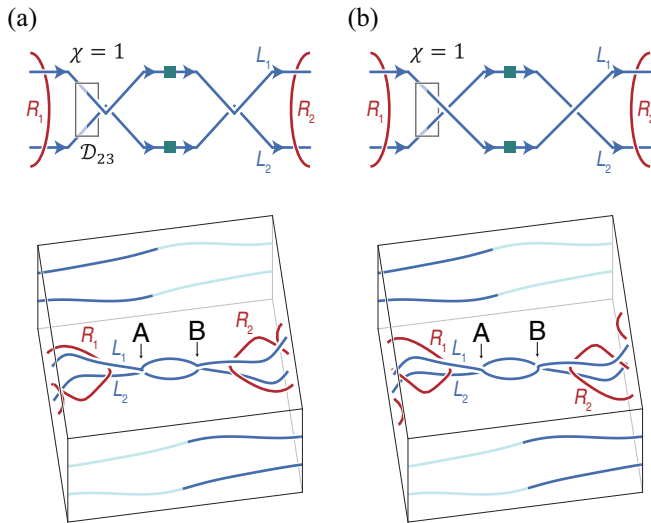


FIG. 4. Allowed transition of nodal lines L_1 and L_2 according to the Euler class. L_1 and L_2 carry the same frame charge which gives Euler class of $+1$ for \mathcal{D}_{23} .

calculated from \mathbf{u}_k^1 and \mathbf{u}_k^2 over \mathcal{D}_{12} , denoted by $\chi_{12}(\mathcal{D}_{12})$, is $+2$. This indicates that the four nodal lines of R_1 and R_2 piercing through \mathcal{D}_{12} are stable, and their orientations are commonly outward of the surface. Any two of these four are not annihilated on \mathcal{D}_{12} until R_3 and R_4 are annihilated, like in Figs. 3(a)–3(c).

Let us consider another cube that wraps R_2 and name its surface \mathcal{D}_{23} [refer Fig. 2(f)]. R_3 and R_4 pass through the left and right patches of \mathcal{D}_{23} , respectively, while R_1 and R_2 do not touch \mathcal{D}_{23} . The total Euler class $\chi_{23}(\mathcal{D}_{23})$ is zero, and this means that R_3 and R_4 can merge together. In detail, the zero-valued total Euler class is due to the cancellation of the Euler classes on the left and right patches of \mathcal{D}_{23} . The two nodal lines' orientations on the one boundary are inward, and the other two are oriented outward on the opposite boundary. Thus the annihilation of R_3 and R_4 can occur only by merging two nodal lines respectively from R_3 and R_4 because their orientations are opposite for the \mathcal{D}_{23} surface. This corresponds to the inverse process from Fig. 3(d) to 3(b). The detailed process of calculating the Euler classes is in Appendix D.

Although the transition of nodal lines has been discussed in Ref. [59], we consider this from the Euler class point of view. Due to the nonzero Euler classes on the left and right faces of \mathcal{D}_{23} in Fig. 2(f), the nodal ring R_3 cannot be separated into two rings in the region between R_1 and R_2 . Instead, two nodal lines in R_3 can touch each other while keeping their orientations. The same explanation is also applied to R_4 . Let us recall Fig. 2(e) and focus on the touching in R_1 . The two nodal lines are heading towards the junction, while the others are departing from the junction. Then we infer a transition that two nodal lines heading in the same direction change their connectivity through nodal chain while keeping the same Euler class, as illustrated in Fig. 4. In this case, the nodal chain where the nodal lines intersect each other can be considered as the critical state. The detailed discussions and results are in Appendix E.

Our spring-mass system is \mathcal{T} -symmetric, thereby the band structure is inversion symmetric about the Γ point throughout

the momentum space. Thus we note that the L_1 and L_2 in Fig. 4 cannot be transformed into a double helix [59,77–81], and R_1 and R_2 in Fig. 3 cannot form a simple Hopf link [26,51,52,58,82] or an ∞ -shaped structure twisted from a single loop, because these structures do not have an inversion symmetry.

VI. CONCLUSIONS

We show that recently predicted multigap topologies and the relation with the stability of nodal lines become of importance in an easily implementable class of spring-mass systems. The on-site springs in our classical system make it possible to generate a nodal link in three-dimensional momentum space. Tuning the intersite spring constants drives the braiding and phase transition of the nodal lines. Finally, the nonzero (zero) Euler class calculated over a patch indicates that the nodal lines in the patch are stable (unstable). Our system thus provides a platform for these novel pursuits. Indeed, we note that a spring-mass system with two masses in a unit cell, which has six bands, can be a good platform for four-band models [21,22], allowing for more diverse braiding processes and multigap topologies. Furthermore, adjusting spring constants is easier than selecting materials with appropriate elastic moduli in a continuum scale problem because a spring constant is simply determined by material properties and geometrical factors. Therefore we hope that our system can give an impetus to further explore experimental realization of multigap topologies.

ACKNOWLEDGMENTS

The work by H.P., S.W., and S.S.O. has been funded by the European Regional Development Fund through the Welsh Government (80762-CU145, East). A.B. is funded by a Marie Skłodowska-Curie fellowship, Grant No. 101025315. R.J.S. acknowledges funding from a New Investigator Award, EP-SRC Grant No. EP/W00187X/1, as well as Trinity College, Cambridge.

APPENDIX A: 3×3 EIGENVALUE PROBLEM FOR SPRING-MASS SYSTEM

1. Spring forces for spring-mass system

In this section the general form of the Hamiltonian for the three-dimensional spring-mass system is derived. The unit cell of our spring-mass system for phononic modes consists of one mass m and several massless springs, as displayed in Fig. 5(a). The type of the lattice system, i.e., whether it is triclinic, monoclinic, orthorhombic, tetragonal, rhombohedral, hexagonal, or cubic, is determined by the lattice vectors, \mathbf{a}_1 , \mathbf{a}_2 , and \mathbf{a}_3 . The springs are classified as two groups: intersite and on-site. The intersite springs connect the masses in adjacent unit cells. Their spring constants are denoted as C_{ii} , C_{ij} , and C_{ijk} , as illustrated in Figs. 5(b)–5(e). The subscript ii means that the spring is placed along \mathbf{a}_i so that it connects the first-nearest-neighbor masses. The subscript ij ($ij = 12, 23, 31, \bar{1}\bar{2}, \bar{2}\bar{3}, \bar{3}\bar{1}$) indicates the second-nearest-neighbor connection along $\mathbf{a}_i + \mathbf{a}_j$ (if $j > 0$) or $\mathbf{a}_i - \mathbf{a}_j$ (if $j < 0$) [see Figs. 5(b)–5(d)]. C_{123} , $C_{\bar{1}\bar{2}\bar{3}}$, and $C_{1\bar{2}\bar{3}}$ indicate the spring constants of the springs that connect the third-nearest-neighbor masses along the directions $\mathbf{a}_1 + \mathbf{a}_2 + \mathbf{a}_3$, $-\mathbf{a}_1 + \mathbf{a}_2 + \mathbf{a}_3$, $\mathbf{a}_1 - \mathbf{a}_2 + \mathbf{a}_3$, and

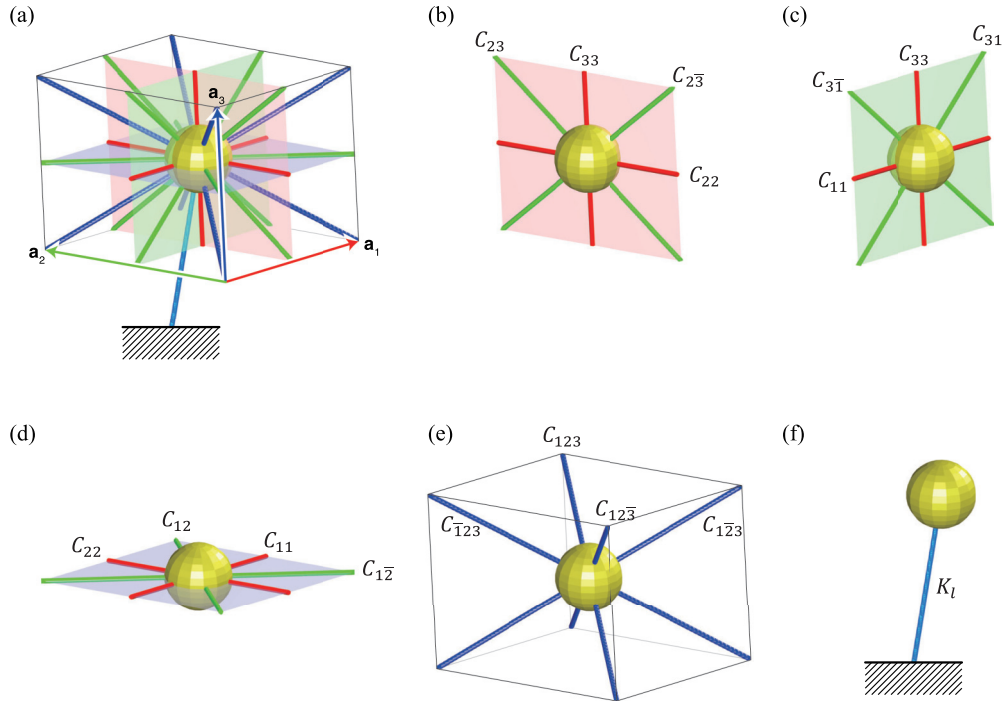


FIG. 5. Generalized spring-mass system. (a) Unit cell containing a mass and all springs dealt in the generalized 3×3 matrix. (b)–(d) Mass and springs on the red, green, and blue planes in (a), respectively. (e) Mass and springs along the diagonal directions of the unit cell. (f) Schematic figure of the spring concerning on-site potential.

$\mathbf{a}_1 + \mathbf{a}_2 - \mathbf{a}_3$, respectively [see Fig. 5(e)]. The on-site springs connect the mass and a nonvibrating fixed point. Their spring constants are denoted by K_l ($l = 1, 2, \dots, N$), and the number of the on-site springs has no limit in our model. We use $N = 2$ throughout this study.

To derive the equation of motion for three-dimensional infinite array, we denote a particular unit cell by an integer-valued vector $[h_1, h_2, h_3]$, where each component is the index along \mathbf{a}_1 , \mathbf{a}_2 , and \mathbf{a}_3 directions, respectively. Then, for instance, a unit cell $[h_1, h_2, h_3 + 1]$ means the next cell to the cell $[h_1, h_2, h_3]$ along the \mathbf{a}_3 direction. For the mass's displacement $\mathbf{u}_{h_1, h_2, h_3}$ in the current unit cell, the equation of motion is

$$m\ddot{\mathbf{u}}_{h_1, h_2, h_3} = \sum_{i=1}^3 \mathbf{f}_i^{1st} + \sum_{i,j} \mathbf{f}_{ij}^{2nd} + \sum_{i,j,k} \mathbf{f}_{ijk}^{3rd} + \sum_l \mathbf{f}_l^0, \quad (\text{A1})$$

$$\mathbf{f}_1^{1st} = \{C_{11}(\mathbf{u}_{h_1+1, h_2, h_3} - \mathbf{u}_{h_1, h_2, h_3}) \cdot \hat{\mathbf{a}}_1\} \hat{\mathbf{a}}_1 + \{C_{11}(\mathbf{u}_{h_1-1, h_2, h_3} - \mathbf{u}_{h_1, h_2, h_3}) \cdot \hat{\mathbf{a}}_1\} \hat{\mathbf{a}}_1. \quad (\text{A2a})$$

Likewise, the net spring forces between the first-nearest-neighbors along $\hat{\mathbf{a}}_2$ and $\hat{\mathbf{a}}_3$ directions are respectively expressed as

$$\begin{aligned} \mathbf{f}_2^{1st} &= \{C_{22}(\mathbf{u}_{h_1, h_2+1, h_3} - \mathbf{u}_{h_1, h_2, h_3}) \cdot \hat{\mathbf{a}}_2\} \hat{\mathbf{a}}_2 + \{C_{22}(\mathbf{u}_{h_1, h_2-1, h_3} - \mathbf{u}_{h_1, h_2, h_3}) \cdot \hat{\mathbf{a}}_2\} \hat{\mathbf{a}}_2 \\ \mathbf{f}_3^{1st} &= \{C_{33}(\mathbf{u}_{h_1, h_2, h_3+1} - \mathbf{u}_{h_1, h_2, h_3}) \cdot \hat{\mathbf{a}}_3\} \hat{\mathbf{a}}_3 + \{C_{33}(\mathbf{u}_{h_1, h_2, h_3-1} - \mathbf{u}_{h_1, h_2, h_3}) \cdot \hat{\mathbf{a}}_3\} \hat{\mathbf{a}}_3. \end{aligned} \quad (\text{A2b})$$

For the second-nearest-neighbors, we should consider six directions, $\hat{\mathbf{a}}_{12}$, $\hat{\mathbf{a}}_{1\bar{2}}$, $\hat{\mathbf{a}}_{23}$, $\hat{\mathbf{a}}_{2\bar{3}}$, $\hat{\mathbf{a}}_{31}$, and $\hat{\mathbf{a}}_{3\bar{1}}$, where $\hat{\mathbf{a}}_{ij}$ and $\hat{\mathbf{a}}_{i\bar{j}}$ are the unit vectors in $\mathbf{a}_i + \mathbf{a}_j$ and $\mathbf{a}_i - \mathbf{a}_j$ directions, respectively. Then the spring forces between the second-nearest-neighbors \mathbf{f}_{ij}^{2nd} are given by

$$\mathbf{f}_{12}^{2nd} = \{C_{12}(\mathbf{u}_{h_1+1, h_2+1, h_3} - \mathbf{u}_{h_1, h_2, h_3}) \cdot \hat{\mathbf{a}}_{12}\} \hat{\mathbf{a}}_{12} + \{C_{12}(\mathbf{u}_{h_1-1, h_2-1, h_3} - \mathbf{u}_{h_1, h_2, h_3}) \cdot \hat{\mathbf{a}}_{12}\} \hat{\mathbf{a}}_{12} \quad (\text{A2c})$$

$$\mathbf{f}_{1\bar{2}}^{2nd} = \{C_{1\bar{2}}(\mathbf{u}_{h_1+1, h_2-1, h_3} - \mathbf{u}_{h_1, h_2, h_3}) \cdot \hat{\mathbf{a}}_{1\bar{2}}\} \hat{\mathbf{a}}_{1\bar{2}} + \{C_{1\bar{2}}(\mathbf{u}_{h_1-1, h_2+1, h_3} - \mathbf{u}_{h_1, h_2, h_3}) \cdot \hat{\mathbf{a}}_{1\bar{2}}\} \hat{\mathbf{a}}_{1\bar{2}} \quad (\text{A2d})$$

$$\mathbf{f}_{23}^{2nd} = \{C_{23}(\mathbf{u}_{h_1, h_2+1, h_3+1} - \mathbf{u}_{h_1, h_2, h_3}) \cdot \hat{\mathbf{a}}_{23}\} \hat{\mathbf{a}}_{23} + \{C_{23}(\mathbf{u}_{h_1, h_2-1, h_3-1} - \mathbf{u}_{h_1, h_2, h_3}) \cdot \hat{\mathbf{a}}_{23}\} \hat{\mathbf{a}}_{23} \quad (\text{A2e})$$

$$\mathbf{f}_{23}^{2nd} = \{C_{23}(\mathbf{u}_{h_1, h_2+1, h_3-1} - \mathbf{u}_{h_1, h_2, h_3}) \cdot \hat{\mathbf{a}}_{23}\} \hat{\mathbf{a}}_{23} + \{C_{23}(\mathbf{u}_{h_1, h_2-1, h_3+1} - \mathbf{u}_{h_1, h_2, h_3}) \cdot \hat{\mathbf{a}}_{23}\} \hat{\mathbf{a}}_{23} \quad (\text{A2f})$$

$$\mathbf{f}_{31}^{2nd} = \{C_{31}(\mathbf{u}_{h_1+1, h_2, h_3+1} - \mathbf{u}_{h_1, h_2, h_3}) \cdot \hat{\mathbf{a}}_{31}\} \hat{\mathbf{a}}_{31} + \{C_{31}(\mathbf{u}_{h_1-1, h_2, h_3-1} - \mathbf{u}_{h_1, h_2, h_3}) \cdot \hat{\mathbf{a}}_{31}\} \hat{\mathbf{a}}_{31} \quad (\text{A2g})$$

$$\mathbf{f}_{3\bar{1}}^{2nd} = \{C_{3\bar{1}}(\mathbf{u}_{h_1-1, h_2, h_3+1} - \mathbf{u}_{h_1, h_2, h_3}) \cdot \hat{\mathbf{a}}_{3\bar{1}}\} \hat{\mathbf{a}}_{3\bar{1}} + \{C_{3\bar{1}}(\mathbf{u}_{h_1+1, h_2, h_3-1} - \mathbf{u}_{h_1, h_2, h_3}) \cdot \hat{\mathbf{a}}_{3\bar{1}}\} \hat{\mathbf{a}}_{3\bar{1}}. \quad (\text{A2h})$$

There are four directions connecting the third-nearest-neighbors, $\hat{\mathbf{a}}_{123}$, $\hat{\mathbf{a}}_{\bar{1}23}$, $\hat{\mathbf{a}}_{1\bar{2}3}$, and $\hat{\mathbf{a}}_{\bar{1}\bar{2}3}$, which are the unit vectors along the directions $\mathbf{a}_1 + \mathbf{a}_2 + \mathbf{a}_3$, $-\mathbf{a}_1 + \mathbf{a}_2 + \mathbf{a}_3$, $\mathbf{a}_1 - \mathbf{a}_2 + \mathbf{a}_3$, and $\mathbf{a}_1 + \mathbf{a}_2 - \mathbf{a}_3$, respectively. Then the spring forces between the third nearest neighbors \mathbf{f}_{ijk}^{3rd} are written as

$$\mathbf{f}_{123}^{3rd} = \{C_{123}(\mathbf{u}_{h_1+1, h_2+1, h_3+1} - \mathbf{u}_{h_1, h_2, h_3}) \cdot \hat{\mathbf{a}}_{123}\} \hat{\mathbf{a}}_{123} + \{C_{123}(\mathbf{u}_{h_1-1, h_2-1, h_3-1} - \mathbf{u}_{h_1, h_2, h_3}) \cdot \hat{\mathbf{a}}_{123}\} \hat{\mathbf{a}}_{123} \quad (\text{A2i})$$

$$\mathbf{f}_{\bar{1}23}^{3rd} = \{C_{\bar{1}23}(\mathbf{u}_{h_1-1, h_2+1, h_3+1} - \mathbf{u}_{h_1, h_2, h_3}) \cdot \hat{\mathbf{a}}_{\bar{1}23}\} \hat{\mathbf{a}}_{\bar{1}23} + \{C_{\bar{1}23}(\mathbf{u}_{h_1+1, h_2-1, h_3-1} - \mathbf{u}_{h_1, h_2, h_3}) \cdot \hat{\mathbf{a}}_{\bar{1}23}\} \hat{\mathbf{a}}_{\bar{1}23} \quad (\text{A2j})$$

$$\mathbf{f}_{1\bar{2}3}^{3rd} = \{C_{1\bar{2}3}(\mathbf{u}_{h_1+1, h_2-1, h_3+1} - \mathbf{u}_{h_1, h_2, h_3}) \cdot \hat{\mathbf{a}}_{1\bar{2}3}\} \hat{\mathbf{a}}_{1\bar{2}3} + \{C_{1\bar{2}3}(\mathbf{u}_{h_1-1, h_2+1, h_3-1} - \mathbf{u}_{h_1, h_2, h_3}) \cdot \hat{\mathbf{a}}_{1\bar{2}3}\} \hat{\mathbf{a}}_{1\bar{2}3} \quad (\text{A2k})$$

$$\mathbf{f}_{\bar{1}\bar{2}3}^{3rd} = \{C_{\bar{1}\bar{2}3}(\mathbf{u}_{h_1+1, h_2+1, h_3-1} - \mathbf{u}_{h_1, h_2, h_3}) \cdot \hat{\mathbf{a}}_{\bar{1}\bar{2}3}\} \hat{\mathbf{a}}_{\bar{1}\bar{2}3} + \{C_{\bar{1}\bar{2}3}(\mathbf{u}_{h_1-1, h_2-1, h_3+1} - \mathbf{u}_{h_1, h_2, h_3}) \cdot \hat{\mathbf{a}}_{\bar{1}\bar{2}3}\} \hat{\mathbf{a}}_{\bar{1}\bar{2}3}. \quad (\text{A2l})$$

We also describe the spring force corresponding to the on-site energy. By considering the current cell $[h_1, h_2, h_3]$ only, the spring force \mathbf{f}_l^0 in Eq. (A1) is written as

$$\mathbf{f}_l^0 = -K_l(\hat{\mathbf{d}}_l \otimes \hat{\mathbf{d}}_l)\mathbf{u}_{h_1, h_2, h_3}, \quad (\text{A2m})$$

where $\hat{\mathbf{d}}_l = \mathbf{d}_l/|\mathbf{d}_l|$ is the unit vector along the spring connection, and \otimes is the outer product.

Equations (A2) are summed to give the summations in Eq. (A1):

$$\sum_{i=1}^3 \mathbf{f}_i^{1st} = \mathbf{f}_1^{1st} + \mathbf{f}_2^{1st} + \mathbf{f}_3^{1st} \quad (\text{A3a})$$

$$\sum_{i,j} \mathbf{f}_{ij}^{2nd} = \mathbf{f}_{12}^{2nd} + \mathbf{f}_{1\bar{2}}^{2nd} + \mathbf{f}_{23}^{2nd} + \mathbf{f}_{\bar{2}3}^{2nd} + \mathbf{f}_{31}^{2nd} + \mathbf{f}_{3\bar{1}}^{2nd} \quad (\text{A3b})$$

$$\sum_{i,j,k} \mathbf{f}_{ijk}^{3rd} = \mathbf{f}_{123}^{3rd} + \mathbf{f}_{\bar{1}23}^{3rd} + \mathbf{f}_{1\bar{2}3}^{3rd} + \mathbf{f}_{\bar{1}\bar{2}3}^{3rd} \quad (\text{A3c})$$

$$\sum_l \mathbf{f}_l^0 = \mathbf{f}_1^0 + \mathbf{f}_2^0 + \dots \quad (\text{A3d})$$

2. Derivation of the Hamiltonian for spring-mass system

Owing to translation symmetry, the displacement vector can be expressed as $\mathbf{u}_{h_1, h_2, h_3}(\mathbf{x}, t) = \mathbf{u}_{\mathbf{k}} e^{i\mathbf{k}\cdot\mathbf{x}} e^{-i\omega t} =$

$\mathbf{u}_{\mathbf{k}} e^{i\mathbf{k}\cdot(h_1\mathbf{a}_1 + h_2\mathbf{a}_2 + h_3\mathbf{a}_3)} e^{-i\omega t}$. We substitute this into the following equation, which is just oppositely signed of Eq. (A1):

$$-m\ddot{\mathbf{u}}_{h_1, h_2, h_3} = -\sum_{i=1}^3 \mathbf{f}_i^{1st} - \sum_{i,j} \mathbf{f}_{ij}^{2nd} - \sum_{i,j,k} \mathbf{f}_{ijk}^{3rd} - \sum_l \mathbf{f}_l^0. \quad (\text{A4})$$

The left-hand side becomes

$$-m\ddot{\mathbf{u}}_{h_1, h_2, h_3} = m\omega^2 \mathbf{u}_{\mathbf{k}} e^{i\mathbf{k}\cdot\mathbf{x}} e^{-i\omega t}. \quad (\text{A5})$$

To get the results for the first three terms in the right-hand side, we input the above $\mathbf{u}_{h_1, h_2, h_3}(\mathbf{x}, t)$ into Eqs. (A2). For example, $-\mathbf{f}_1^{1st}$ becomes

$$\begin{aligned} -\mathbf{f}_1^{1st} &= -\{C_{11}(\mathbf{u}_{h_1+1, h_2, h_3} + \mathbf{u}_{h_1-1, h_2, h_3} - 2\mathbf{u}_{h_1, h_2, h_3}) \cdot \hat{\mathbf{a}}_1\} \hat{\mathbf{a}}_1 \\ &= -\{C_{11}(e^{i\mathbf{k}\cdot\mathbf{a}_1} + e^{-i\mathbf{k}\cdot\mathbf{a}_1} - 2)\mathbf{u}_{h_1, h_2, h_3} \cdot \hat{\mathbf{a}}_1\} \hat{\mathbf{a}}_1 e^{i\mathbf{k}\cdot\mathbf{x}} e^{-i\omega t} \\ &= 2C_{11}\{1 - \cos(\mathbf{k} \cdot \mathbf{a}_1)\}(\mathbf{u}_{\mathbf{k}} \cdot \hat{\mathbf{a}}_1)\hat{\mathbf{a}}_1 e^{i\mathbf{k}\cdot\mathbf{x}} e^{-i\omega t}. \end{aligned} \quad (\text{A6})$$

Using $(\mathbf{u}_{\mathbf{k}} \cdot \hat{\mathbf{a}}_1)\hat{\mathbf{a}}_1 = (\hat{\mathbf{a}}_1 \otimes \hat{\mathbf{a}}_1)\mathbf{u}_{\mathbf{k}}$ (which results from the vector identity $(\mathbf{v} \cdot \mathbf{w})\mathbf{w} = v_i w_i w_j = w_j w_i v_i = (\mathbf{w} \otimes \mathbf{w})\mathbf{v}$), the above equation becomes

$$-\mathbf{f}_1^{1st} = 2C_{11}\{1 - \cos(\mathbf{k} \cdot \mathbf{a}_1)\}(\hat{\mathbf{a}}_1 \otimes \hat{\mathbf{a}}_1)\mathbf{u}_{\mathbf{k}} e^{i\mathbf{k}\cdot\mathbf{x}} e^{-i\omega t}. \quad (\text{A7a})$$

We also convert the other spring forces in Eqs. (A2) as follows:

$$-\mathbf{f}_2^{1st} = 2C_{22}\{1 - \cos(\mathbf{k} \cdot \mathbf{a}_2)\}(\hat{\mathbf{a}}_2 \otimes \hat{\mathbf{a}}_2)\mathbf{u}_{\mathbf{k}} e^{i\mathbf{k}\cdot\mathbf{x}} e^{-i\omega t} \quad (\text{A7b})$$

$$-\mathbf{f}_3^{1st} = 2C_{33}\{1 - \cos(\mathbf{k} \cdot \mathbf{a}_3)\}(\hat{\mathbf{a}}_3 \otimes \hat{\mathbf{a}}_3)\mathbf{u}_{\mathbf{k}} e^{i\mathbf{k}\cdot\mathbf{x}} e^{-i\omega t} \quad (\text{A7c})$$

$$-\mathbf{f}_{12}^{2nd} = 2C_{12}\{1 - \cos(\mathbf{k} \cdot \mathbf{a}_1 + \mathbf{k} \cdot \mathbf{a}_2)\}(\hat{\mathbf{a}}_{12} \otimes \hat{\mathbf{a}}_{12})\mathbf{u}_{\mathbf{k}} e^{i\mathbf{k}\cdot\mathbf{x}} e^{-i\omega t} \quad (\text{A7d})$$

$$-\mathbf{f}_{\bar{1}2}^{2nd} = 2C_{\bar{1}2}\{1 - \cos(\mathbf{k} \cdot \mathbf{a}_1 - \mathbf{k} \cdot \mathbf{a}_2)\}(\hat{\mathbf{a}}_{\bar{1}2} \otimes \hat{\mathbf{a}}_{\bar{1}2})\mathbf{u}_{\mathbf{k}} e^{i\mathbf{k}\cdot\mathbf{x}} e^{-i\omega t} \quad (\text{A7e})$$

$$-\mathbf{f}_{23}^{2nd} = 2C_{23}\{1 - \cos(\mathbf{k} \cdot \mathbf{a}_2 + \mathbf{k} \cdot \mathbf{a}_3)\}(\hat{\mathbf{a}}_{23} \otimes \hat{\mathbf{a}}_{23})\mathbf{u}_{\mathbf{k}} e^{i\mathbf{k}\cdot\mathbf{x}} e^{-i\omega t} \quad (\text{A7f})$$

$$-\mathbf{f}_{\bar{2}3}^{2nd} = 2C_{\bar{2}3}\{1 - \cos(\mathbf{k} \cdot \mathbf{a}_2 - \mathbf{k} \cdot \mathbf{a}_3)\}(\hat{\mathbf{a}}_{\bar{2}3} \otimes \hat{\mathbf{a}}_{\bar{2}3})\mathbf{u}_{\mathbf{k}} e^{i\mathbf{k}\cdot\mathbf{x}} e^{-i\omega t} \quad (\text{A7g})$$

$$-\mathbf{f}_{31}^{2nd} = 2C_{31}\{1 - \cos(\mathbf{k} \cdot \mathbf{a}_3 + \mathbf{k} \cdot \mathbf{a}_1)\}(\hat{\mathbf{a}}_{31} \otimes \hat{\mathbf{a}}_{31})\mathbf{u}_{\mathbf{k}} e^{i\mathbf{k}\cdot\mathbf{x}} e^{-i\omega t} \quad (\text{A7h})$$

$$-\mathbf{f}_{3\bar{1}}^{2nd} = 2C_{3\bar{1}}\{1 - \cos(\mathbf{k} \cdot \mathbf{a}_3 - \mathbf{k} \cdot \mathbf{a}_1)\}(\hat{\mathbf{a}}_{3\bar{1}} \otimes \hat{\mathbf{a}}_{3\bar{1}})\mathbf{u}_{\mathbf{k}} e^{i\mathbf{k}\cdot\mathbf{x}} e^{-i\omega t} \quad (\text{A7i})$$

$$-\mathbf{f}_l^0 = -K_l(\hat{\mathbf{d}}_l \otimes \hat{\mathbf{d}}_l)\mathbf{u}_{\mathbf{k}} e^{i\mathbf{k}\cdot\mathbf{x}} e^{-i\omega t}. \quad (\text{A7j})$$

TABLE I. Parameter sets to realize the nodal links shown in Fig. 6. The mass m in Eq. (A8b) is set as 1.

Lattice system	Parameter sets
Triclinic	$\mathbf{a}_1 = [1, 0, 0], \mathbf{a}_2 = [-0.5, 1.0825, 0], \mathbf{a}_3 = [-0.3, -0.2, 1]$ $C_{11} = 30, C_{22} = 110, C_{33} = 280$ $C_{12} = 95, C_{1\bar{2}} = 55, C_{23} = 62, C_{2\bar{3}} = 42, C_{31} = 40, C_{3\bar{1}} = 30$ $C_{123} = 50, C_{1\bar{2}3} = 0, C_{1\bar{2}\bar{3}} = 30, C_{12\bar{3}} = 0$ $K_1 = 40, \mathbf{d}_1 = \mathbf{a}_1$ $K_2 = 180, \mathbf{d}_2 = 0.3924\mathbf{a}_1 + 0.1848\mathbf{a}_2 + 1.0\mathbf{a}_3$
Monoclinic	$\mathbf{a}_1 = [1, 0, 0], \mathbf{a}_2 = [0, 1.2, 0], \mathbf{a}_3 = [0, -0.2, 1]$ $C_{11} = 30, C_{22} = 110, C_{33} = 280$ $C_{12} = 95, C_{1\bar{2}} = 55, C_{23} = 62, C_{2\bar{3}} = 42, C_{31} = 40, C_{3\bar{1}} = 30$ $C_{123} = 0, C_{1\bar{2}3} = 0, C_{1\bar{2}\bar{3}} = 0, C_{12\bar{3}} = 20$ $K_1 = 40, \mathbf{d}_1 = \mathbf{a}_1$ $K_2 = 180, \mathbf{d}_2 = 0.1667\mathbf{a}_2 + 1.0\mathbf{a}_3$
Orthorhombic	$\mathbf{a}_1 = [1, 0, 0], \mathbf{a}_2 = [0, 1.1, 0], \mathbf{a}_3 = [0, 0, 1.2]$ $C_{11} = 30, C_{22} = 110, C_{33} = 280$ $C_{12} = 95, C_{1\bar{2}} = 55, C_{23} = 26, C_{2\bar{3}} = 26, C_{31} = 40, C_{3\bar{1}} = 30$ $C_{123} = 0, C_{1\bar{2}3} = 0, C_{1\bar{2}\bar{3}} = 0, C_{12\bar{3}} = 0$ $K_1 = 40, \mathbf{d}_1 = \mathbf{a}_2$ $K_2 = 160, \mathbf{d}_2 = \mathbf{a}_3$
Tetragonal	$\mathbf{a}_1 = [1, 0, 0], \mathbf{a}_2 = [0, 1, 0], \mathbf{a}_3 = [0, 0, 1.2]$ $C_{11} = 30, C_{22} = 110, C_{33} = 280$ $C_{12} = 95, C_{1\bar{2}} = 55, C_{23} = 52, C_{2\bar{3}} = 52, C_{31} = 40, C_{3\bar{1}} = 30$ $C_{123} = 0, C_{1\bar{2}3} = 0, C_{1\bar{2}\bar{3}} = 0, C_{12\bar{3}} = 0$ $K_1 = 40, \mathbf{d}_1 = \mathbf{a}_2$ $K_2 = 160, \mathbf{d}_2 = \mathbf{a}_3$
Rhombohedral	$\mathbf{a}_1 = [1, 0, 0.438], \mathbf{a}_2 = [-1/2, \sqrt{3}/2, 0.438], \mathbf{a}_3 = [-1/2, -\sqrt{3}/2, 0.438]$ $C_{11} = 30, C_{22} = 110, C_{33} = 280$ $C_{12} = 95, C_{1\bar{2}} = 55, C_{23} = 85, C_{2\bar{3}} = 35, C_{31} = 40, C_{3\bar{1}} = 30$ $C_{123} = 70, C_{1\bar{2}3} = 0, C_{1\bar{2}\bar{3}} = 25, C_{12\bar{3}} = 0$ $K_1 = 40, \mathbf{d}_1 = \mathbf{a}_2 - \mathbf{a}_3$ $K_2 = 160, \mathbf{d}_2 = \mathbf{a}_1 + \mathbf{a}_2 + \mathbf{a}_3$
Hexagonal	$\mathbf{a}_1 = [1/2, -\sqrt{3}/2, 0], \mathbf{a}_2 = [1/2, \sqrt{3}/2, 0], \mathbf{a}_3 = [0, 0, 1.5]$ $C_{11} = 30, C_{22} = 110, C_{33} = 280$ $C_{12} = 95, C_{1\bar{2}} = 55, C_{23} = 26, C_{2\bar{3}} = 26, C_{31} = 40, C_{3\bar{1}} = 30$ $C_{123} = 35, C_{1\bar{2}3} = 10, C_{1\bar{2}\bar{3}} = 0, C_{12\bar{3}} = 65$ $K_1 = 260, \mathbf{d}_1 = \mathbf{a}_1 + \mathbf{a}_2$ $K_2 = 160, \mathbf{d}_2 = \mathbf{a}_3$
Cubic	$\mathbf{a}_1 = [1, 0, 0], \mathbf{a}_2 = [0, 1, 0], \mathbf{a}_3 = [0, 0, 1]$ $C_{11} = 30, C_{22} = 110, C_{33} = 280$ $C_{12} = 80, C_{1\bar{2}} = 80, C_{23} = 26, C_{2\bar{3}} = 26, C_{31} = 40, C_{3\bar{1}} = 30$ $C_{123} = 35, C_{1\bar{2}3} = 10, C_{1\bar{2}\bar{3}} = 0, C_{12\bar{3}} = 65$ $K_1 = 60, \mathbf{d}_1 = \mathbf{a}_2$ $K_2 = 240, \mathbf{d}_2 = \mathbf{a}_3$

By replacing all terms in Eq. (A4) as Eqs. (A7) and dropping $e^{i\mathbf{k}\cdot\mathbf{x}}e^{-i\omega t}$, we finally get

$$H\mathbf{u}_{\mathbf{k}} = \omega^2\mathbf{u}_{\mathbf{k}}. \quad (\text{A8a})$$

Here, the real-valued 3×3 Hamiltonian H is given by

$$\begin{aligned}
 H = \frac{2}{m} & \left[C_{11}\{1 - \cos(\mathbf{k} \cdot \mathbf{a}_1)\}\hat{\mathbf{a}}_1 \otimes \hat{\mathbf{a}}_1 + C_{22}\{1 - \cos(\mathbf{k} \cdot \mathbf{a}_2)\}\hat{\mathbf{a}}_2 \otimes \hat{\mathbf{a}}_2 + C_{33}\{1 - \cos(\mathbf{k} \cdot \mathbf{a}_3)\}\hat{\mathbf{a}}_3 \otimes \hat{\mathbf{a}}_3 \right. \\
 & + C_{12}\{1 - \cos(\mathbf{k} \cdot \mathbf{a}_1 + \mathbf{k} \cdot \mathbf{a}_2)\}\hat{\mathbf{a}}_{12} \otimes \hat{\mathbf{a}}_{12} + C_{1\bar{2}}\{1 - \cos(\mathbf{k} \cdot \mathbf{a}_1 - \mathbf{k} \cdot \mathbf{a}_2)\}\hat{\mathbf{a}}_{1\bar{2}} \otimes \hat{\mathbf{a}}_{1\bar{2}} \\
 & + C_{23}\{1 - \cos(\mathbf{k} \cdot \mathbf{a}_2 + \mathbf{k} \cdot \mathbf{a}_3)\}\hat{\mathbf{a}}_{23} \otimes \hat{\mathbf{a}}_{23} + C_{2\bar{3}}\{1 - \cos(\mathbf{k} \cdot \mathbf{a}_2 - \mathbf{k} \cdot \mathbf{a}_3)\}\hat{\mathbf{a}}_{2\bar{3}} \otimes \hat{\mathbf{a}}_{2\bar{3}} \\
 & \left. + C_{31}\{1 - \cos(\mathbf{k} \cdot \mathbf{a}_3 + \mathbf{k} \cdot \mathbf{a}_1)\}\hat{\mathbf{a}}_{31} \otimes \hat{\mathbf{a}}_{31} + C_{3\bar{1}}\{1 - \cos(\mathbf{k} \cdot \mathbf{a}_3 - \mathbf{k} \cdot \mathbf{a}_1)\}\hat{\mathbf{a}}_{3\bar{1}} \otimes \hat{\mathbf{a}}_{3\bar{1}} \right]
 \end{aligned}$$

$$\begin{aligned}
& + C_{123}\{1 - \cos(\mathbf{k} \cdot \mathbf{a}_1 + \mathbf{k} \cdot \mathbf{a}_2 + \mathbf{k} \cdot \mathbf{a}_3)\}\hat{\mathbf{a}}_{123} \otimes \hat{\mathbf{a}}_{123} + C_{\bar{1}23}\{1 - \cos(-\mathbf{k} \cdot \mathbf{a}_1 + \mathbf{k} \cdot \mathbf{a}_2 + \mathbf{k} \cdot \mathbf{a}_3)\}\hat{\mathbf{a}}_{\bar{1}23} \otimes \hat{\mathbf{a}}_{\bar{1}23} \\
& + C_{1\bar{2}3}\{1 - \cos(\mathbf{k} \cdot \mathbf{a}_1 - \mathbf{k} \cdot \mathbf{a}_2 + \mathbf{k} \cdot \mathbf{a}_3)\}\hat{\mathbf{a}}_{1\bar{2}3} \otimes \hat{\mathbf{a}}_{1\bar{2}3} + C_{12\bar{3}}\{1 - \cos(\mathbf{k} \cdot \mathbf{a}_1 + \mathbf{k} \cdot \mathbf{a}_2 - \mathbf{k} \cdot \mathbf{a}_3)\}\hat{\mathbf{a}}_{12\bar{3}} \otimes \hat{\mathbf{a}}_{12\bar{3}} \\
& + \frac{1}{2} \sum_l K_l (\hat{\mathbf{d}}_l \otimes \hat{\mathbf{d}}_l) \Big]. \tag{A8b}
\end{aligned}$$

All terms in the right-hand side of the above equation are written as $\mathbf{n} \otimes \mathbf{n}$ form. Thus, Hamiltonian H is symmetric and positive definite for any wave vector \mathbf{k} . Its eigenstates $\mathbf{u}_{\mathbf{k}}^1$, $\mathbf{u}_{\mathbf{k}}^2$, and $\mathbf{u}_{\mathbf{k}}^3$ form an SO(3) orthonormal frame.

The orthorhombic system in the main text does not have H_{ijk} because all the spring constants C_{123} , $C_{\bar{1}23}$, $C_{1\bar{2}3}$, and $C_{12\bar{3}}$ are zero, as shown in Table I.

APPENDIX B: NODAL LINKS IN SEVEN LATTICE SYSTEMS

In this section the seven lattice systems containing a single mass in a unit cell are considered. The input parameters for Eq. (A8) are lattice vectors [see Fig. 5(a)], 13 intersite spring constants [see Figs. 5(b)–5(e)], and information of on-site springs including the spring constants K_l and the directions $\hat{\mathbf{d}}_l$ [see Fig. 5(f)]. For each lattice system defined by \mathbf{a}_1 , \mathbf{a}_2 , and \mathbf{a}_3 , the parameter sets to realize the nodal links are listed in Table I. The real space systems by those parameters and the resulting nodal links in momentum space are shown in the left and right figures in each panel of Fig. 6. The red and blue nodal lines are the degeneracies by $\omega_{\mathbf{k}}^2 - \omega_{\mathbf{k}}^1$ and $\omega_{\mathbf{k}}^3 - \omega_{\mathbf{k}}^2$, respectively. In all cases, the blue-colored nodal rings encircle the Γ point, the other blue-colored nodal rings span the first Brillouin boundaries, two red-colored nodal rings exist around the Γ point, and these red and blue nodal rings are infinitely connected to reveal the nodal links.

All the seven cases have two on-site springs. In each case, the two constants K_1 and K_2 of these springs are different. These make the eigenfrequencies of the 3×3 Hamiltonian H [Eq. (A8b)] different at the Γ point. Two nodal rings R_1 and R_2 do not intersect each other at this point, and the triple-point degeneracy is also not observed here.

The triclinic, monoclinic, rhombohedral, hexagonal, and cubic cases have at least one spring for the third-nearest-neighbor springs, and their values in each case are different (see Table I). Furthermore, in all cases except the cubic lattice, C_{12} and $C_{\bar{1}2}$ are different, and C_{31} and $C_{\bar{3}1}$ also have different values. These spring constants make the lattice have no rotation or mirror symmetries. They preserve \mathcal{P} symmetry and \mathcal{T} symmetry only.

APPENDIX C: FRAME CHARGES

1. Charges $\pm k$ and $\pm i$ of nodal lines

In the main text, the frame charge of the nodal line by the first and second (by the second and third) bands were denoted as $\pm k$ ($\pm i$) among $\mathbb{Q} = \{\pm i, \pm j, \pm k, -1, +1\}$. In this section we see how they can be achieved and briefly review the frame charge [21–24,26]. We select the orthorhombic system shown in the main text [or in Fig. 6(c)] as an example. First we investigate the frame charge of the nodal ring R_2 . We consider a closed loop parametrized by $\alpha \in [0, 2\pi]$ encircling R_2 , as shown in the right inset of Fig. 7(a). Along the loop, the eigenstates $\mathbf{u}_{\mathbf{k}}^1$, $\mathbf{u}_{\mathbf{k}}^2$, and $\mathbf{u}_{\mathbf{k}}^3$ are calculated [see Fig. 7(b)] where the superscripts are the band numbers. The tails of all the eigenstates are collected at the origin of an arbitrary

orthogonal coordinate system, for example, the $\mathbf{u}_{\mathbf{k}_0}^1$ – $\mathbf{u}_{\mathbf{k}_0}^2$ – $\mathbf{u}_{\mathbf{k}_0}^3$ coordinate system [see Fig. 7(c)]. The eigenstates reveal that all the $\mathbf{u}_{\mathbf{k}}^3$ s for $\alpha \in [0, 2\pi]$ are fixed along one direction while $\mathbf{u}_{\mathbf{k}}^1$ and $\mathbf{u}_{\mathbf{k}}^2$ exhibit $+\pi$ rotations. The rotation matrix for these behaviors is $R_{12}(\alpha) = e^{(\alpha/2)L_3}$, where $(L_i)_{jk} = -\varepsilon_{ijk}$. Rewriting $R_{12}(\alpha)$ by its lift in the double cover Spin(3) gives $\bar{R}_{12}(\alpha) = e^{-i(\alpha/2)(\sigma_3/2)}$ with $\alpha \in [0, 4\pi]$ [23,55]. Therefore, $\bar{R}_{12}(\alpha = 2\pi) = -i\sigma_3$, and the frame charge of Figs. 7(b)–7(c) is the quaternion number k [23,54,55]. The same analysis can be used to the loop that encloses R_3 in Fig. 7(a). After calculating the eigenstates along the loop [see Fig. 7(d)], the rotation matrix for the results in Fig. 7(e) is $R_{23}(\alpha) = e^{(\alpha/2)L_1}$, and lifting in the double cover Spin(3) gives $\bar{R}_{23}(\alpha) = e^{-i(\alpha/2)(\sigma_1/2)}$. Therefore we get $\bar{R}_{23}(\alpha = 2\pi) = -i\sigma_1$, indicating the frame charge i [23,54,55].

The results on the frame charges $\pm k$ and $\pm i$ [shown in Figs. 7(c) and 7(e)] show that the eigenstates of the adjacent two bands concerning the nodal line commonly show the π disclination, that is, the signs of the eigenstates at $\mathbf{k}(\alpha = 0)$ and $\mathbf{k}(\alpha = 2\pi)$ are opposite. The eigenstates of the remaining bands do not exhibit π disclination. Then we observe the rotation of the former two sets of the eigenstates by π around the latter sets of the eigenstates. As already mentioned, the frame charges are determined by which bands show the π disclinations and which band is fixed.

2. Stability/instability of nodal lines, and their braiding

In this section we analyze the behavior of nodal lines in Fig. 3 in the main text using the frame charges. The following discussions provide further insight in understanding Figs. 2 and 3 in the main text.

The frame charges -1 and $+1$ provide useful information on the stability/instability of nodal lines, as the Euler class does [23,26]. To characterize nodal lines' stability/instability, a closed loop that encircles even number of nodal lines is placed. We suppose the right-handed rule; if one nodal line's frame charge is positive, its orientation is the thumb's direction when we grab the line along the closed loop's direction. The same (opposite) frame charges indicate that the total frame charge is -1 ($+1$), their orientations are the same (opposite), and they are stable (can be pair-annihilated).

The frame charge calculated along the loop C_1 in Fig. 8(a) is -1 , meaning that L_1 and L_2 have the same orientations. C_1 is not placed through R_1 and R_2 . If R_1 and R_2 grow as shown in Fig. 3(b) in the main text, and if C_1 still does not pass through these two rings (or C_1 detours the rings), the frame charge remains -1 . However, if the closed loop C_1 is set as shown in

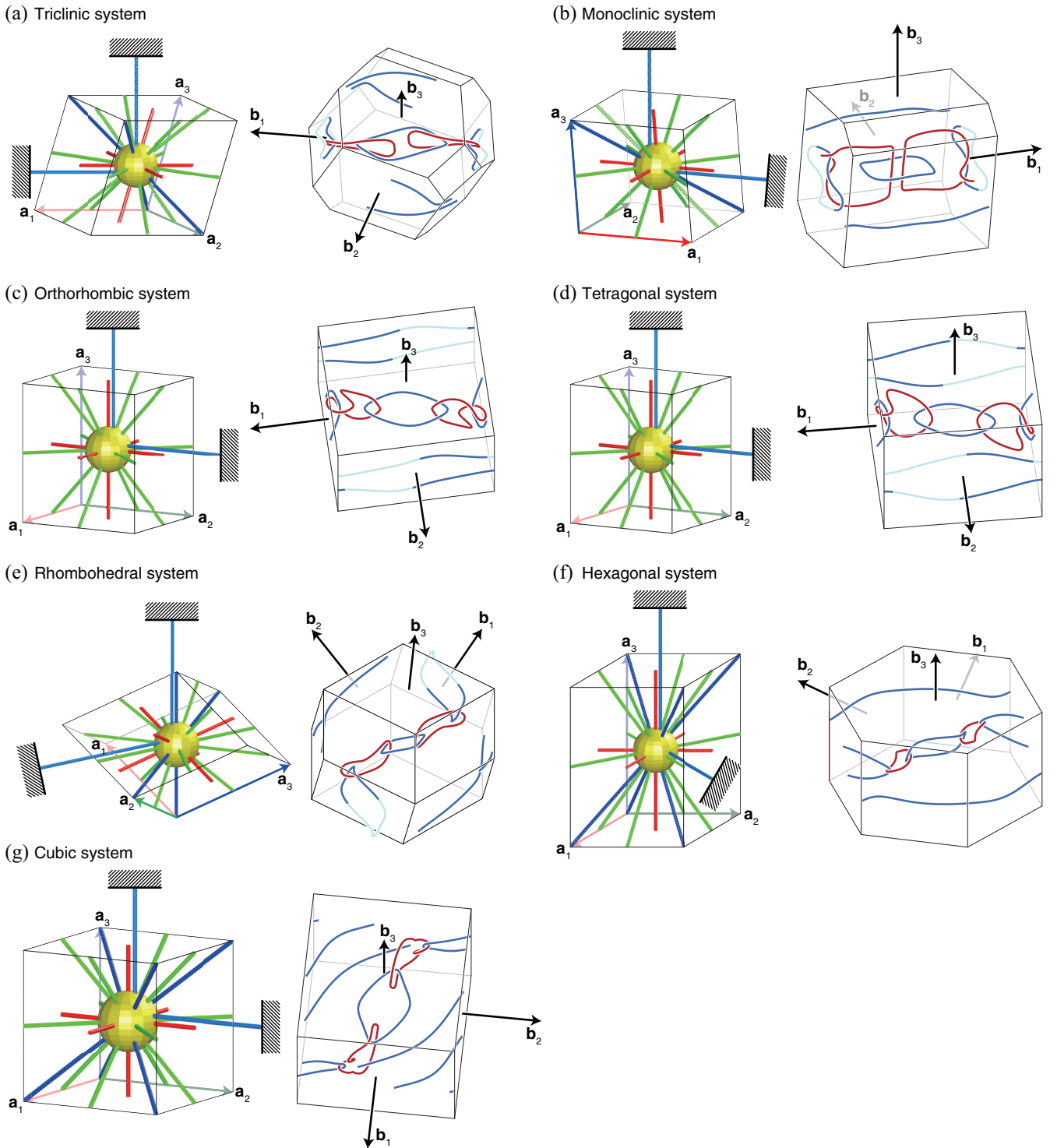


FIG. 6. Seven lattice systems and their nodal links. The left figures in each panel are the real space plots according to Table I. The spring whose spring constant is zero is not plotted. The right figures in each panel are the resulting nodal links in the first Brillouin zones. The red and blue nodal lines are by $\omega_k^2 - \omega_k^1$ and $\omega_k^3 - \omega_k^2$, respectively. The light blue nodal lines around boundaries mean that they are outside the current Brillouin zone. (c) is equivalent to Fig. 3(d) in the main text.

Fig. 8(b) [as illustrated in Fig. 2(d) in the main text], the frame charge becomes +1, the trivial case, so that they can transform into the nodal chain and nodal link in Figs. 3(c) and 3(d) in the main text.

Meanwhile, we investigate the frame charge of R_2 . For the loop C_2 in Fig. 8(c), the frame charge is +1, so that R_2 can

be deformed to shrink and disappear if it follows the path drawn by C_2 , like Fig. 8(a). However, if we consider a loop C_3 that detours both L_1 and L_2 [see Fig. 8(d)], the frame charge becomes -1: R_2 cannot be deformed to disappear if it follows the path by C_3 . After deforming L_1 and L_2 into R_3 and R_4 , the relation between C_3 and R_2 remains [see Fig. 8(e)]. Thus the

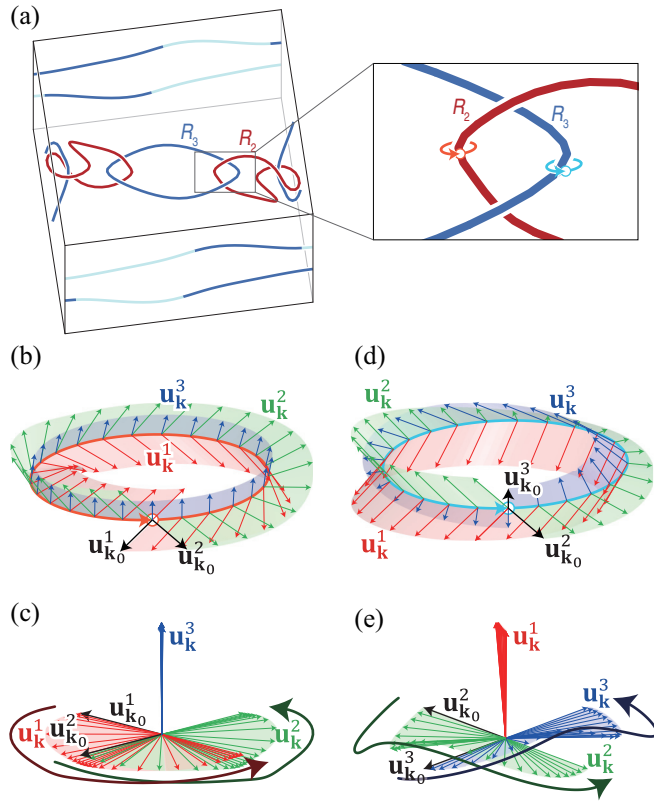


FIG. 7. Frame charges k and i of the orthorhombic system. (a) Closed loops that encircle the nodal rings R_2 and R_3 , respectively. (b), (d) Eigenstates \mathbf{u}_k^1 , \mathbf{u}_k^2 , and \mathbf{u}_k^3 on the loops in (a), respectively, in an arbitrary coordinate system. (c), (e) Eigenstates whose tails are gathered at the origin. In (c), the dark-red and -green curved arrows mean the traces of the eigenstates \mathbf{u}_k^1 and \mathbf{u}_k^2 rotating around \mathbf{u}_k^3 , respectively. In (f) the dark-green and -blue curved arrows mean the traces of the eigenstates \mathbf{u}_k^2 and \mathbf{u}_k^3 rotating around \mathbf{u}_k^1 , respectively.

frame charge is -1 , and R_2 becomes stable. The frame charge of R_1 can be explained in the same manner.

3. Consistency between frame charges and Euler classes of the nodal link

This section discusses the stability and instability of the nodal rings R_1 - R_2 and R_3 - R_4 using the frame charges. Results generated in this section are consistent with the analyses using Euler classes that will be mentioned in Secs. D 2 and D 3. First we set a loop C_4 tying R_1 and R_2 , as shown in Fig. 8(f). The frame charge calculated along C_4 is -1 . This means that the orientations of both R_1 and R_2 are the right-handed outward directions of the C_4 surface. As already mentioned regarding Fig. 8(e), two nodal lines of R_2 are outward of the C_3 surface. The situation of R_1 is the same. Therefore all four nodal lines of R_1 and R_2 apart from the Γ point are commonly outward.

The situation of the nodal rings R_3 and R_4 is different. The charges along both C_5 and C_6 in Fig. 8(g) are -1 ; thus the same charges are generated in each ring R_3 and R_4 . However, on the surface of the loop C_7 in Fig. 8(h), the orientations of R_3 and R_4 are opposite because the frame charge obtained along C_7 is $+1$. Therefore R_3 and R_4 are not stable regarding the C_7 connection.

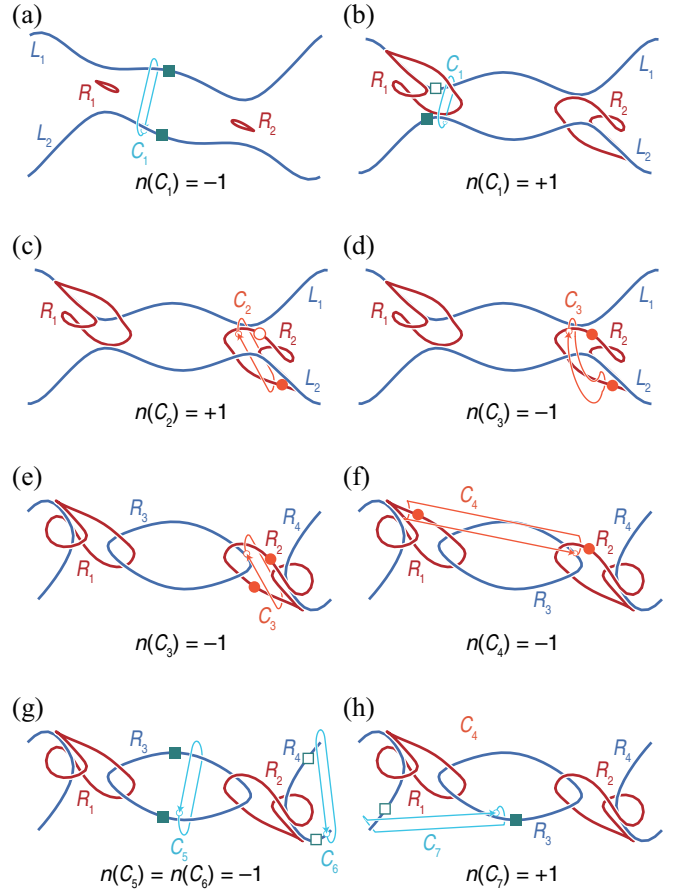


FIG. 8. Nodal lines and closed loops for frame charge characterizations. Nodal lines in (a), (b)–(d), and (e)–(f) correspond to Figs. 3(a), 3(b) and 3(d), respectively. Frame charges $n(C_i)$ calculated on each loop C_i are also denoted. Note that the open and solid symbols (circles and rectangles) do not mean the absolute frame charge of each nodal line, but they are shown to illustrate the same or opposite orientations between two nodal lines enclosed by a closed loop.

APPENDIX D: EULER CLASS

1. Euler form and Euler class

For real eigenstates $|u_k^m\rangle$ and $|u_k^n\rangle$ of any two adjacent bands m and n , the Euler form is given by

$$\text{Eu}^{mn}(\mathbf{k}) = \langle \nabla_{\mathbf{k}} u_k^m | \times | \nabla_{\mathbf{k}} u_k^n \rangle. \quad (\text{D1})$$

The Euler class, an integer topological invariant, is given by [24,25,27–30]

$$\chi_{mn}(\mathcal{D}) = \frac{1}{2\pi} \left[\int_{\mathcal{D}} \text{Eu}^{mn} dk_a dk_b - \oint_{\partial \mathcal{D}} \mathbf{a}(\mathbf{k}) \cdot d\mathbf{k} \right], \quad (\text{D2})$$

where $\mathbf{a}(\mathbf{k}) = \langle u_k^m | \nabla_{\mathbf{k}} u_k^n \rangle$ is the Euler connection. The Euler class is the difference between the surface integral of the Euler form over a patch \mathcal{D} and the boundary integral of the Euler connection. If there is no nodal line passing through the patch, this surface can be filled with smooth $|u_k^m\rangle$. By Stokes' theorem, Eq. (D2) becomes zero. If the patch is pierced by a nodal line, the intersecting point becomes a singularity, and Eq. (D2) is not zero.

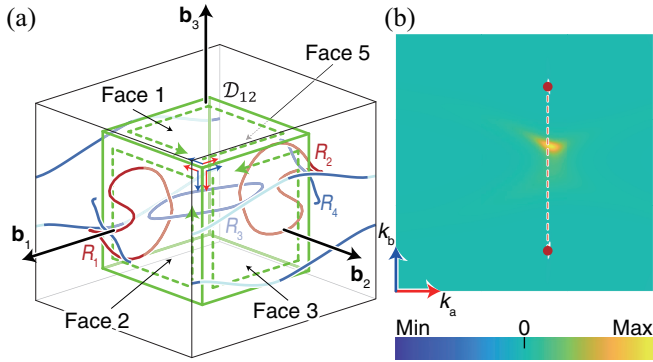


FIG. 9. Calculation of Euler class $\chi_{12}(\mathcal{D}_{12})$. (a) Patch \mathcal{D}_{12} pierced by R_1 and R_2 . Local coordinates k_a and k_b for each face are also marked as red and blue arrows. $k_a \times k_b$ is always outward of the box. The integral of Euler connection is performed along the counterclockwise direction of each boundary, as displayed by the green dotted arrows. (b) Euler form numerically calculated over face 2 of \mathcal{D}_{12} . The red dots indicate the nodal lines, and the dotted lines are the Dirac strings. The yellowish region is a result of the region being near the curved section of R_1 , as shown in (a). Face 5's Euler form is the same. On the other faces, the surface integral of Euler form and boundary integral of Euler connection are canceled out.

2. Euler class for R_1 and R_2 in the nodal link

In the momentum space of our orthorhombic spring-mass system, two nodal rings R_1 and R_2 , degeneracies by $\omega_{\mathbf{k}}^2 - \omega_{\mathbf{k}}^1$, are generated, as shown in Fig. 3 in the main text. To calculate the Euler class, we set a cubic patch centered on the Γ point, denoted by \mathcal{D}_{12} [see Fig. 9(a)]. The patch completely encloses R_3 , degeneracies by $\omega_{\mathbf{k}}^3 - \omega_{\mathbf{k}}^2$. In other words, there is no nodal line by $\omega_{\mathbf{k}}^3 - \omega_{\mathbf{k}}^2$ passing the \mathcal{D}_{12} surface. Only R_1 and R_2 intersect this surface.

We divide \mathcal{D}_{12} into six square faces. To calculate the surface integral of Eq. (D2) for each face, k_a and k_b in Eq. (D2) are set such that $k_a \times k_b$ is outward of the cube. Each face contains zero or even number of nodal line piercings. If a face contains the piercings, (i) we skip calculating Eq. (D2) around the nodal lines where the eigenstates are not sufficiently continuous, and (ii) the eigenstates' gauge are adjusted to make them smooth across Dirac string. We also calculate the boundary integral in Eq. (D2). The summation of the boundary integral for all the edges of the cube should be zero because all the paths in Fig. 9(a) are canceled out. By using this we adjust the signs of Euler classes over the six faces to make the boundary integral summation zero.

The Euler form for Face 2 in Fig. 9(a) is shown in Fig. 9(b). Face 2 has two piercings, and its Euler class is +1. Thus the two nodal lines are stable, and they have the same orientations. Face 5 exhibits the same results. For Faces 1 and 3, Euler classes, the sum of the surface integral of the Euler form and boundary integral of the Euler connection are zero. Thus the overall result $\chi_{12}(\mathcal{D}_{12})$ becomes +2.

The above analysis only reveals the summation of Euler classes over \mathcal{D}_{12} 's six faces; it does not show a direct result of Euler class by R_1 and R_2 . Thus we lower Face 1's position along the $-\mathbf{b}_3$ direction to make it contain two nodal lines by R_1 and R_2 , respectively. In this case, the Euler class calculated over Face 1 is +1, and we can ensure that all the nodal lines of

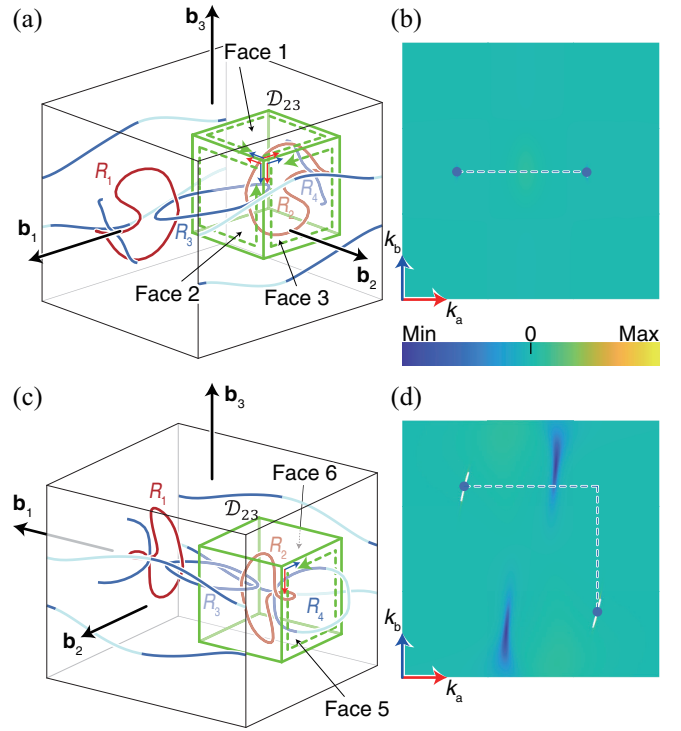


FIG. 10. Calculation of Euler class $\chi_{23}(\mathcal{D}_{23})$. (a), (c) Patch \mathcal{D}_{23} pierced by R_3 and R_4 . (b), (d) Euler form numerically calculated over faces 2 and 5 of \mathcal{D}_{23} , respectively. The blue dots indicate the nodal lines, and the dotted line is the Dirac string. On the other faces of \mathcal{D}_{23} , the surface integral of Euler form and boundary integral of the Euler connection are canceled out.

R_1 and R_2 are outward of \mathcal{D}_{12} . All the results in this section are consistent with Figs. 8(e) and 8(f) in Sec. C 2.

3. Euler class for R_3 and R_4 in the nodal link

The nodal link mentioned in the previous section also reveals the nodal rings R_3 and R_4 , degeneracies by $\omega_{\mathbf{k}}^3 - \omega_{\mathbf{k}}^2$. We set a box \mathcal{D}_{23} that contains R_2 . Only R_3 and R_4 intersect this patch through Faces 2 and 5 [see Figs. 10(a) and 10(c)]. We calculate the Euler class in Eq. (D2) for all six faces of the box by considering the same things as in the previous section. Euler classes for Faces 2 and 5 are +1 and -1, respectively. Another four faces exhibit the zero-valued Euler class. Thus the total result $\chi_{23}(\mathcal{D}_{23})$ is 0, and therefore the transition between Figs. 3(c) and 3(d) is possible.

Because both Euler classes calculated over Faces 2 and 5 are nonzero, the two nodal lines of a single ring escaping the same face of the box cannot be annihilated. Thus the transition of R_3 and R_4 to nodal lines L_1 and L_2 in Fig. 3(c) in the main text is done by annihilation of each strand of R_3 and R_4 . This can be more clearly seen if we pull Face 6 in Fig. 10(c) (the face parallel to \mathbf{b}_1 and \mathbf{b}_3) along \mathbf{b}_2 direction so that it contains totally two degeneracies that respectively belong to R_3 and R_4 ; its Euler class is zero. All these discussions are consistent with Figs. 8(g) and 8(h) in Sec. C 2.

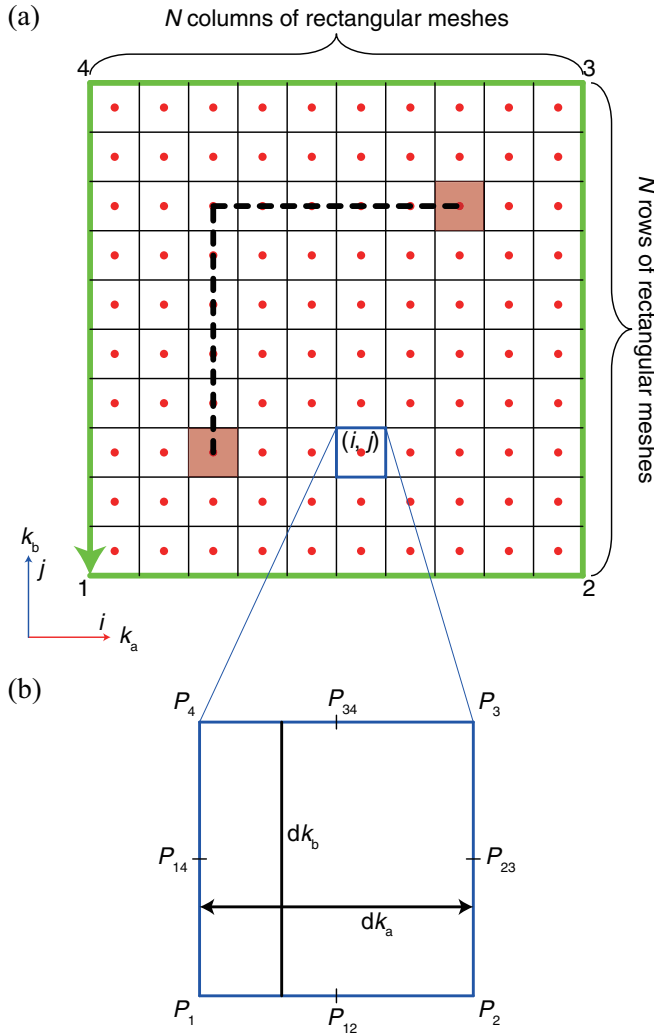


FIG. 11. Schematics of calculating Euler class. (a) Discretized domain to calculate the Euler class. This domain consists of N^2 rectangular meshes. Eigenfrequencies and eigenstates are calculated at red dots and meshes' vertices, respectively. Meshes that contain band degeneracies are marked as red rectangles. The thick dotted black path means the Dirac string. Each mesh is indexed by (i, j) . Eigenstates smoothing on the boundary and Euler connection integral are performed along the thick green arrow direction. (b) Enlarged cell (i, j) . P_{12} , P_{23} , P_{34} , and P_{14} are midpoints of each edge.

4. Numerical calculation of the Euler class

Throughout this study we use a two-dimensional surface as a domain to calculate the Euler class Eq. (D2). We assume that a domain contains zero or two degeneracies, and we also suppose that we already know whether the domain has degeneracies from a plot of nodal lines. Thus the rough positions of degeneracies are given input parameters. The degeneracies are by $\omega_{\mathbf{k}}^n - \omega_{\mathbf{k}}^m$ ($n > m$), and there are not any other degeneracies by $\omega_{\mathbf{k}}^m - \omega_{\mathbf{k}}^{m-1}$ or $\omega_{\mathbf{k}}^{n+1} - \omega_{\mathbf{k}}^n$. As Eq. (D2) consists of a surface and boundary integrals, we also divide the numerical process into two parts: numerical calculation over the surface and along the boundary.

To perform the surface integral, we prepare $N \times N$ rectangular meshes on the domain, as shown in Fig. 11(a). On

the domain we can think of two sets of points: one group of vertices of the meshes, and the other group of the meshes' central points marked as red dots in Fig. 11(a). The number of points in the first and second groups are $(N + 1)^2$ and N^2 , respectively.

Next we calculate eigenfrequencies using Eq. (A8) at the red dots of Fig. 11(a) to search which meshes have the band degeneracies. The aforementioned input parameters, the degeneracies' rough positions, are used here. We regard that a degeneracy is in a mesh if the mesh is around one of the degeneracies' rough position, and if $\Delta\omega_{mn} = \omega_{\mathbf{k}}^n - \omega_{\mathbf{k}}^m$ at the mesh is minimum compared to surrounding meshes. After determining two meshes of degeneracies, we define a Dirac string that connects the two meshes [see the dotted path in Fig. 11(a)]. The Dirac string can take various routes, but we use the simple path that bends one time at most.

The eigenstates $\mathbf{u}_{\mathbf{k}}^1$, $\mathbf{u}_{\mathbf{k}}^2$, and $\mathbf{u}_{\mathbf{k}}^3$ of Eq. (A8) are then calculated at the vertices of all the meshes. At each point the eigenstates should satisfy the right-handed rule $\mathbf{u}_{\mathbf{k}}^1 \cdot (\mathbf{u}_{\mathbf{k}}^2 \times \mathbf{u}_{\mathbf{k}}^3) = +1$. Practically, we use the condition $\mathbf{u}_{\mathbf{k}}^1 \cdot (\mathbf{u}_{\mathbf{k}}^2 \times \mathbf{u}_{\mathbf{k}}^3) \geq 0$ considering the numerical errors.

All the eigenstates should be smoothed by adjusting their gauges (determining their signs). First we make them continuous along the boundary in the counterclockwise directions, as marked with the green arrow in Fig. 11(a). Then the smoothing process is carried out from the boundary to the inner regions of the domain. This smoothing should not go across the Dirac string. Thus all the smoothing processes stop in the vicinity of the Dirac string.

To calculate the Euler form in Eq. (D1), we mark four vertices of a mesh as P_1 , P_2 , P_3 , P_4 , as shown in Fig. 11(b). In the previous steps the eigenstates $\mathbf{u}_{\mathbf{k}}^m$ and $\mathbf{v}_{\mathbf{k}}^n$ at these points are already prepared. Let us denote $\mathbf{u}_{\mathbf{k}}^m$ as \mathbf{U}_{P_1} , \mathbf{U}_{P_2} , \mathbf{U}_{P_3} , and \mathbf{U}_{P_4} . Likewise, $\mathbf{v}_{\mathbf{k}}^n$ is also rewritten as \mathbf{V}_{P_1} , \mathbf{V}_{P_2} , \mathbf{V}_{P_3} , and \mathbf{V}_{P_4} . If the current mesh is on the Dirac string, the eigenstates at P_2 , P_3 , P_4 should be smoothed using the eigenstates at P_1 . On each edge of the mesh, we set midpoints P_{12} , P_{23} , P_{34} , P_{14} , as denoted in Fig. 11(b). The eigenstates \mathbf{U} and \mathbf{V} at each midpoint are obtained from their averages at both ends of the edge. The Euler form in Eq. (D1) is now rewritten as

$$\begin{aligned} \text{Eu} = & \frac{\mathbf{U}_{P_{23}} - \mathbf{U}_{P_{14}}}{dk_a} \cdot \frac{\mathbf{V}_{P_{34}} - \mathbf{V}_{P_{12}}}{dk_b} \\ & - \frac{\mathbf{U}_{P_{34}} - \mathbf{U}_{P_{12}}}{dk_b} \cdot \frac{\mathbf{V}_{P_{23}} - \mathbf{V}_{P_{14}}}{dk_a}, \end{aligned} \quad (\text{D3})$$

where $dk_a = |P_{23} - P_{14}|$ and $dk_b = |P_{34} - P_{12}|$ are the edges' lengths of the mesh. With the mesh's area $dA = |P_2 - P_1| |P_4 - P_1|$, we sum up all the Euler form in Eq. (D3) as follows:

$$\int_{\mathcal{D}} \text{Eu} dk_a dk_b = \sum_{i,j} \text{Eu}_{ij} dA_{ij}, \quad (\text{D4})$$

where i and j are each mesh's indices from the left to right and bottom to top in Fig. 11(a), respectively. If the current mesh has a degeneracy or is around a degeneracy where the eigenstates are ill defined (that is, if at least one pair among \mathbf{U}_{P_1} to \mathbf{U}_{P_4} has the inner product below the tolerance 0.99), Eu_{ij} in this mesh is not summed to the above equation by assigning zero to Eu_{ij} .

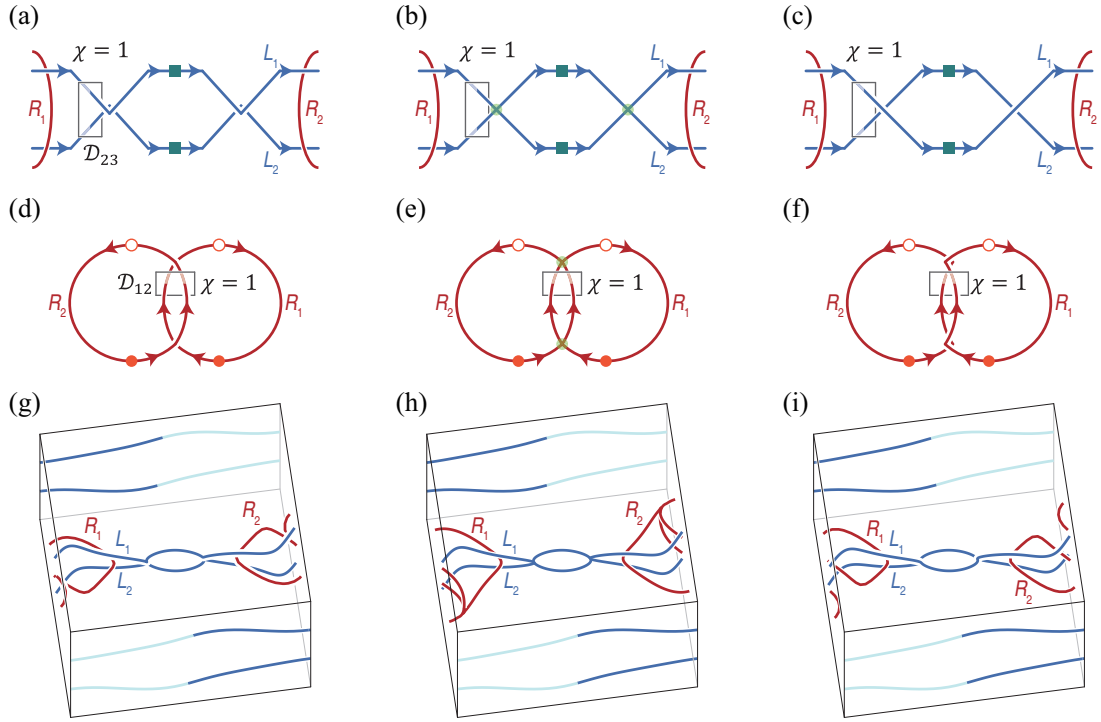


FIG. 12. Allowed transition of nodal lines and nodal rings between (a), (d), (g) and (c), (f), (i), through (b), (e), (h). Schematics (a)–(c) are about the transition of nodal lines L_1 and L_2 . Schematics (d)–(f) display the transition of R_1 and R_2 on the zone boundary. If R_2 is in the current zone, R_1 is in the next zone. (g)–(i) Realization of (a)–(c) and (d)–(f) using the spring-mass system. The transition is performed by decreasing ΔC_{31} from 2 (g) through 0 (h) to -2 (i), with setting $K_1 = 140$ and keeping the other variables in Table I.

Meanwhile, we use the smoothed eigenstates on the boundary to calculate the boundary integral of Eq. (D2). We rewrite the boundary integral as follows:

$$\oint_{\partial\mathcal{D}} \langle u_{\mathbf{k}}^m | \nabla_{\mathbf{k}} u_{\mathbf{k}}^n \rangle \cdot d\mathbf{k} = \oint_{\partial\mathcal{D}} \mathbf{U} \cdot \frac{\partial \mathbf{V}}{\partial k} dk. \quad (\text{D5})$$

The boundary has four vertices. At any points except for those on the vertices, $\partial \mathbf{V} / \partial k = D\mathbf{V}$ is performed by the two- or four-point central difference method, i.e., $D\mathbf{V}_i = (\mathbf{V}_{i+1} - \mathbf{V}_{i-1})/h$ or $D\mathbf{V}_i = (-\mathbf{V}_{i+2} + 8\mathbf{V}_{i+1} - 8\mathbf{V}_{i-1} + \mathbf{V}_{i-2})/12h$, respectively, where h is the spacing between adjacent points. At the beginning and finishing vertices, marked as 1 in Fig. 11(a), the three-point forward and backward differences are used, respectively, i.e., $D\mathbf{V}_i = (-3\mathbf{V}_i + 4\mathbf{V}_{i+1} - \mathbf{V}_{i+2})/2h$ and $D\mathbf{V}_i = (\mathbf{V}_{i-2} - 4\mathbf{V}_{i-1} + 3\mathbf{V}_i)/2h$, respectively. At vertices 2, 3, and 4, both three-point forward and backward differences are calculated followed by averaging them. Then the integral in Eq. (D5) becomes

$$\oint_{\partial\mathcal{D}} \mathbf{U} \cdot \frac{\partial \mathbf{V}}{\partial k} dk = \sum_i \mathbf{U}_i \cdot D\mathbf{V}_i h. \quad (\text{D6})$$

Thus the difference between Eqs. (D4) and (D6) generates the final result of the Euler class:

$$\chi = \frac{1}{2\pi} \left[\sum_{i,j} \text{Eu}_{ij} dA_{ij} - \sum_i \mathbf{U}_i \cdot D\mathbf{V}_i h \right]. \quad (\text{D7})$$

We set $N = 600$ throughout this study, that is, a domain consists of 600×600 meshes. The eigenstates are calculated at 601×601 vertices of meshes.

APPENDIX E: TRANSITION FROM NODAL LINK

In the main text we infer the allowed transition, that is, two nodal lines heading the same direction [L_1 and L_2 in Fig. 12(a)] can change their connectivity with keeping the $+1$ Euler class. During this transition from Figs. 12(a)–12(c), a critical state is given by a nodal chain, as shown in Fig. 12(b).

Similar predictions can be made for the nodal rings R_1 and R_2 . At the Brillouin zone boundary, R_2 in the current zone and R_1 in the next zone are getting closer, like Fig. 12(d). The Euler class $\chi(\mathcal{D}_{12})$ over the marked patch in Fig. 12(d) is $+1$. While this condition is satisfied, the nodal rings can be deformed to Figs. 12(e) and 12(f). Here the nodal chain in Fig. 12(e) is the critical state between Figs. 12(d) and 12(f).

Based on the above prediction, we realize these transitions by tuning the spring constants in the spring-mass system. First, from the nodal link in Fig. 3(d) in the main text [or in Fig. 6(c) with Table I], we increase the on-site potential spring K_1 to 140 and decrease ΔC_{31} to 2 (where ΔC_{31} is for control of C_{31} and $C_{3\bar{1}}$ by $C_{31} = C_{31}^0 + \Delta C_{31}$, $C_{3\bar{1}} = C_{31}^0 - \Delta C_{31}$, and $C_{31}^0 = 35$) to prepare Fig. 12(g). Now we decrease ΔC_{31} to zero. Then the spring constants become $C_{31} = C_{3\bar{1}}$, and we have Fig. 12(h). This critical state exhibits two nodal chains formed by L_1 - L_2 around the Γ point and R_1 - R_2 on the zone boundary. Because we have $C_{23} = C_{2\bar{3}}$ and the two on-site springs' directions are respectively the same as \mathbf{a}_2 and \mathbf{a}_3 , this spring-mass system is in $2/m$ (C_{2h}) symmetry. After further decreasing ΔC_{31} to -2 , the nodal chains by L_1 - L_2 and R_1 - R_2 are separated into two nodal lines and nodal rings, respectively

[Fig. 12(i)]. Compared to Fig. 12(g), the connectivity between L_1 and L_2 are exchanged. In addition, R_2 was placed at higher

position along the \mathbf{b}_3 direction than R_1 in Fig. 12(g), and this is now reversed.

-
- [1] X.-L. Qi and S.-C. Zhang, Topological insulators and superconductors, *Rev. Mod. Phys.* **83**, 1057 (2011).
- [2] M. Z. Hasan and C. L. Kane, *Colloquium: Topological insulators*, *Rev. Mod. Phys.* **82**, 3045 (2010).
- [3] N. P. Armitage, E. J. Mele, and A. Vishwanath, Weyl and Dirac semimetals in three-dimensional solids, *Rev. Mod. Phys.* **90**, 015001 (2018).
- [4] L. Fu, Topological Crystalline Insulators, *Phys. Rev. Lett.* **106**, 106802 (2011).
- [5] R.-J. Slager, A. Mesaros, V. Juričić, and J. Zaanen, The space group classification of topological band-insulators, *Nat. Phys.* **9**, 98 (2013).
- [6] B. J. Wieder and B. A. Bernevig, The axion insulator as a pump of fragile topology, [arXiv:1810.02373](https://arxiv.org/abs/1810.02373).
- [7] E. Cornfeld and S. Carmeli, Tenfold topology of crystals: Unified classification of crystalline topological insulators and superconductors, *Phys. Rev. Research* **3**, 013052 (2021).
- [8] G. E. Volovik and V. P. Mineev, Investigation of singularities in superfluid He³ in liquid crystals by the homotopic topology methods, in *Basic Notions of Condensed Matter Physics* (CRC Press, Boca Raton, FL, 2018), pp. 392–401.
- [9] K. Shiozaki and M. Sato, Topology of crystalline insulators and superconductors, *Phys. Rev. B* **90**, 165114 (2014).
- [10] R.-J. Slager, A. Mesaros, V. Juričić, and J. Zaanen, Interplay between electronic topology and crystal symmetry: Dislocation-line modes in topological band insulators, *Phys. Rev. B* **90**, 241403(R) (2014).
- [11] A. Alexandradinata and B. A. Bernevig, Berry-phase description of topological crystalline insulators, *Phys. Rev. B* **93**, 205104 (2016).
- [12] J. Kruthoff, J. de Boer, J. van Wezel, C. L. Kane, and R.-J. Slager, Topological Classification of Crystalline Insulators through Band Structure Combinatorics, *Phys. Rev. X* **7**, 041069 (2017).
- [13] A. J. Beekman, J. Nissinen, K. Wu, K. Liu, R.-J. Slager, Z. Nussinov, V. Cvetkovic, and J. Zaanen, Dual gauge field theory of quantum liquid crystals in two dimensions, *Phys. Rep.* **683**, 1 (2017).
- [14] B. Bradlyn, L. Elcoro, J. Cano, M. G. Vergniory, Z. Wang, C. Felser, M. I. Aroyo, and B. A. Bernevig, Topological quantum chemistry, *Nature (London)* **547**, 298 (2017).
- [15] C. Fang, M. J. Gilbert, and B. A. Bernevig, Bulk topological invariants in noninteracting point group symmetric insulators, *Phys. Rev. B* **86**, 115112 (2012).
- [16] M. S. Scheurer and R.-J. Slager, Unsupervised Machine Learning and Band Topology, *Phys. Rev. Lett.* **124**, 226401 (2020).
- [17] Z. Song, T. Zhang, Z. Fang, and C. Fang, Quantitative mappings between symmetry and topology in solids, *Nat. Commun.* **9**, 1 (2018).
- [18] H. C. Po, A. Vishwanath, and H. Watanabe, Symmetry-based indicators of band topology in the 230 space groups, *Nat. Commun.* **8**, 50 (2017).
- [19] R.-J. Slager, The translational side of topological band insulators, *J. Phys. Chem. Solids* **128**, 24 (2019).
- [20] J. Ahn and B.-J. Yang, Symmetry representation approach to topological invariants in C_{2zt} -symmetric systems, *Phys. Rev. B* **99**, 235125 (2019).
- [21] A. Bouhon, T. Bzdusek, and R.-J. Slager, Geometric approach to fragile topology beyond symmetry indicators, *Phys. Rev. B* **102**, 115135 (2020).
- [22] A. Bouhon and R.-J. Slager, Multi-gap topological conversion of Euler class via band-node braiding: Minimal models, pt -linked nodal rings, and chiral heirs, [arXiv:2203.16741](https://arxiv.org/abs/2203.16741).
- [23] Q. Wu, A. A. Soluyanov, and T. Bzdusek, Non-Abelian band topology in noninteracting metals, *Science* **365**, 1273 (2019).
- [24] A. Bouhon, Q. Wu, R.-J. Slager, H. Weng, O. V. Yazyev, and T. Bzdusek, Non-Abelian reciprocal braiding of Weyl points and its manifestation in ZrTe, *Nat. Phys.* **16**, 1137 (2020).
- [25] J. Ahn, S. Park, and B.-J. Yang, Failure of Nielsen-Ninomiya Theorem and Fragile Topology in Two-Dimensional Systems with Space-Time Inversion Symmetry: Application to Twisted Bilayer Graphene at Magic Angle, *Phys. Rev. X* **9**, 021013 (2019).
- [26] A. Tiwari and T. Bzdusek, Non-Abelian topology of nodal-line rings in \mathcal{PT} -symmetric systems, *Phys. Rev. B* **101**, 195130 (2020).
- [27] B. Jiang, A. Bouhon, Z.-K. Lin, X. Zhou, B. Hou, F. Li, R.-J. Slager, and J.-H. Jiang, Experimental observation of non-Abelian topological acoustic semimetals and their phase transitions, *Nat. Phys.* **17**, 1239 (2021).
- [28] B. Peng, A. Bouhon, B. Monserrat, and R.-J. Slager, Phonons as a platform for non-Abelian braiding and its manifestation in layered silicates, *Nat. Commun.* **13**, 423 (2022).
- [29] A. Bouhon, A. M. Black-Schaffer, and R.-J. Slager, Wilson loop approach to fragile topology of split elementary band representations and topological crystalline insulators with time-reversal symmetry, *Phys. Rev. B* **100**, 195135 (2019).
- [30] F. N. Ünal, A. Bouhon, and R.-J. Slager, Topological Euler Class as a Dynamical Observable in Optical Lattices, *Phys. Rev. Lett.* **125**, 053601 (2020).
- [31] W.-D. Zhao, Y.-B. Yang, Z.-C. M. Y. Jiang, W.-X. Guo, L.-Y. Qiu, G.-X. Wang, L. Yao, L. He, Z.-C. Zhou, Y. Xu, and L.-M. Duan, Observation of topological Euler insulators with a trapped-ion quantum simulator, [arXiv:2201.09234](https://arxiv.org/abs/2201.09234).
- [32] A. Bouhon, G. F. Lange, and R.-J. Slager, Topological correspondence between magnetic space group representations and subdimensions, *Phys. Rev. B* **103**, 245127 (2021).
- [33] S. Chen, A. Bouhon, R.-J. Slager, and B. Monserrat, Non-Abelian braiding of Weyl nodes via symmetry-constrained phase transitions, *Phys. Rev. B* **105**, L081117 (2022).
- [34] V. Könye, A. Bouhon, I. C. Fulga, R.-J. Slager, J. van den Brink, and J. I. Facio, Chirality flip of Weyl nodes and its manifestation in strained MoTe₂, *Phys. Rev. Research* **3**, L042017 (2021).
- [35] B. Peng, A. Bouhon, R.-J. Slager, and B. Monserrat, Multigap topology and non-Abelian braiding of phonons from first principles, *Phys. Rev. B* **105**, 085115 (2022).
- [36] S. Park, Y. Hwang, H. C. Choi, and B.-J. Yang, Topological acoustic triple point, *Nat. Commun.* **12**, 6781 (2021).

- [37] G. F. Lange, A. Bouhon, B. Monserrat, and R.-J. Slager, Topological continuum charges of acoustic phonons in two dimensions and the Nambu-Goldstone theorem, *Phys. Rev. B* **105**, 064301 (2022).
- [38] Y. Takahashi, T. Kariyado, and Y. Hatsugai, Weyl points of mechanical diamond, *Phys. Rev. B* **99**, 024102 (2019).
- [39] Y. Zhou, P. R. Bandaru, and D. F. Sievenpiper, Quantum-spin-Hall topological insulator in a spring-mass system, *New J. Phys.* **20**, 123011 (2018).
- [40] K. Golec, J. F. Palierne, F. Zara, S. Nicolle, and G. Damiand, Hybrid 3d mass-spring system for simulation of isotropic materials with any Poisson's ratio, *The Visual Computer* **36**, 809 (2020).
- [41] M. Kot, Mass spring models of amorphous solids, *ChemEngineering* **5**, 3 (2021).
- [42] X. Yi and S. Liu, Stationary breather model in a two-dimensional hexagonal spring-mass lattice, *Nucl. Phys. B* **951**, 114884 (2020).
- [43] M. Sato, B. E. Hubbard, and A. J. Sievers, Colloquium: Nonlinear energy localization and its manipulation in micromechanical oscillator arrays, *Rev. Mod. Phys.* **78**, 137 (2006).
- [44] X. Yi, J. A. D. Wattis, H. Susanto, and L. J. Cummings, Discrete breathers in a two-dimensional spring-mass lattice, *J. Phys. A: Math. Theor.* **42**, 355207 (2009).
- [45] A. Bandyopadhyay, S. Datta, D. Jana, S. Nath, and M. M. Uddin, The topology and robustness of two Dirac cones in s-graphene: A tight binding approach, *Sci. Rep.* **10**, 2502 (2020).
- [46] H. Park, W. Gao, X. Zhang, and S. S. Oh, Nodal lines in momentum space: Topological invariants and recent realizations in photonic and other systems, *Nanophotonics* **11**, 2779 (2022).
- [47] W. Deng, J. Lu, F. Li, X. Huang, M. Yan, J. Ma, and Z. Liu, Nodal rings and drumhead surface states in phononic crystals, *Nat. Commun.* **10**, 1769 (2019).
- [48] W. Gao, B. Yang, B. Tremain, H. Liu, Q. Guo, L. Xia, A. P. Hibbins, and S. Zhang, Experimental observation of photonic nodal line degeneracies in metacrystals, *Nat. Commun.* **9**, 950 (2018).
- [49] T. Bzdušek, Q. Wu, A. Rüegg, M. Sigrist, and A. A. Soluyanov, Nodal-chain metals, *Nature (London)* **538**, 75 (2016).
- [50] Q. Yan, R. Liu, Z. Yan, B. Liu, H. Chen, Z. Wang, and L. Lu, Experimental discovery of nodal chains, *Nat. Phys.* **14**, 461 (2018).
- [51] G. Chang, S.-Y. Xu, X. Zhou, S.-M. Huang, B. Singh, B. Wang, I. Belopolski, J. Yin, S. Zhang, A. Bansil, H. Lin, and M. Z. Hasan, Topological Hopf and Chain Link Semimetal States and Their Application to Co_2MnGa , *Phys. Rev. Lett.* **119**, 156401 (2017).
- [52] Z. Yan, R. Bi, H. Shen, L. Lu, S.-C. Zhang, and Z. Wang, Nodal-link semimetals, *Phys. Rev. B* **96**, 041103(R) (2017).
- [53] I. Belopolski, K. Manna, D. S. Sanchez, G. Chang, B. Ernst, J. Yin, S. S. Zhang, T. Cochran, N. Shumiya, H. Zheng, B. Singh, G. Bian, D. Multer, M. Litskevich, X. Zhou, S.-M. Huang, B. Wang, T.-R. Chang, S.-Y. Xu, A. Bansil *et al.*, Discovery of topological Weyl fermion lines and drumhead surface states in a room temperature magnet, *Science* **365**, 1278 (2019).
- [54] H. Park, S. Wong, X. Zhang, and S. S. Oh, Non-Abelian charged nodal links in a dielectric photonic crystal, *ACS Photonics* **8**, 2746 (2021).
- [55] E. Yang, B. Yang, O. You, H.-C. Chan, P. Mao, Q. Guo, S. Ma, L. Xia, D. Fan, Y. Xiang, and S. Zhang, Observation of Non-Abelian Nodal Links in Photonics, *Phys. Rev. Lett.* **125**, 033901 (2020).
- [56] P. He, J.-H. Fu, D.-W. Zhang, and S.-L. Zhu, Double exceptional links in a three-dimensional dissipative cold atomic gas, *Phys. Rev. A* **102**, 023308 (2020).
- [57] Y. Xie, J. Cai, J. Kim, P.-Y. Chang, and Y. Chen, Hopf-chain networks evolved from triple points, *Phys. Rev. B* **99**, 165147 (2019).
- [58] C. H. Lee, A. Sutrisno, T. Hofmann, T. Helbig, Y. Liu, Y. S. Ang, L. K. Ang, X. Zhang, M. Greiter, and R. Thomale, Imaging nodal knots in momentum space through topoelectrical circuits, *Nat. Commun.* **11**, 4385 (2020).
- [59] Z. Yang, C.-K. Chiu, C. Fang, and J. Hu, Jones Polynomial and Knot Transitions in Hermitian and Non-Hermitian Topological Semimetals, *Phys. Rev. Lett.* **124**, 186402 (2020).
- [60] M. Wang, S. Liu, Q. Ma, R.-Y. Zhang, D. Wang, Q. Guo, B. Yang, M. Ke, Z. Liu, and C. T. Chan, Experimental observation of non-Abelian earring nodal links in phononic crystals, [arXiv:2106.06711](https://arxiv.org/abs/2106.06711).
- [61] R. Bi, Z. Yan, L. Lu, and Z. Wang, Nodal-knot semimetals, *Phys. Rev. B* **96**, 201305(R) (2017).
- [62] J. Ahn, D. Kim, Y. Kim, and B.-J. Yang, Band Topology and Linking Structure of Nodal Line Semimetals with \mathbb{Z}_2 Monopole Charges, *Phys. Rev. Lett.* **121**, 106403 (2018).
- [63] L. Lu, L. Fu, J. D. Joannopoulos, and M. Soljačić, Weyl points and line nodes in gyroid photonic crystals, *Nat. Photonics* **7**, 294 (2013).
- [64] D. Wang, B. Yang, Q. Guo, R.-Y. Zhang, L. Xia, X. Su, W.-J. Chen, J. Han, S. Zhang, and C. T. Chan, Intrinsic in-plane nodal chain and generalized quaternion charge protected nodal link in photonics, *Light Sci. Appl.* **10**, 83 (2021).
- [65] L. Xia, Q. Guo, B. Yang, J. Han, C.-X. Liu, W. Zhang, and S. Zhang, Observation of Hourglass Nodal Lines in Photonics, *Phys. Rev. Lett.* **122**, 103903 (2019).
- [66] A. Merkel and J. Christensen, Ultrasonic nodal chains in topological granular metamaterials, *Commun. Phys.* **2**, 154 (2019).
- [67] J. Lu, X. Huang, M. Yan, F. Li, W. Deng, and Z. Liu, Nodal-Chain Semimetal States and Topological Focusing in Phononic Crystals, *Phys. Rev. Appl.* **13**, 054080 (2020).
- [68] M. Kot, H. Nagahashi, and P. Szymczak, Elastic moduli of simple mass spring models, *The Visual Computer* **31**, 1339 (2015).
- [69] T. C. Lubensky, C. L. Kane, X. Mao, A. Souslov, and K. Sun, Phonons and elasticity in critically coordinated lattices, *Rep. Prog. Phys.* **78**, 073901 (2015).
- [70] M. Kot and H. Nagahashi, Mass spring models with adjustable Poisson's ratio, *The Visual Computer* **33**, 283 (2017).
- [71] P. A. Pantaleón and Y. Xian, Effects of edge on-site potential in a honeycomb topological magnon insulator, *J. Phys. Soc. Jpn.* **87**, 064005 (2018).
- [72] P. B. Allen and J. Kelner, Evolution of a vibrational wave packet on a disordered chain, *Am. J. Phys.* **66**, 497 (1998).
- [73] G. Gantzounis, M. Serra-Garcia, K. Homma, J. M. Mendoza, and C. Daraio, Granular metamaterials for vibration mitigation, *J. Appl. Phys.* **114**, 093514 (2013).
- [74] E. C. Cuansing, H. Li, and J.-S. Wang, Role of the on-site pinning potential in establishing quasi-steady-state conditions of heat transport in finite quantum systems, *Phys. Rev. E* **86**, 031132 (2012).

- [75] P. M. Lenggenhager, X. Liu, T. Neupert, and T. Bzdušek, Triple nodal points characterized by their nodal-line structure in all magnetic space groups, [arXiv:2201.08404](https://arxiv.org/abs/2201.08404).
- [76] A. A. Burkov, M. D. Hook, and L. Balents, Topological nodal semimetals, *Phys. Rev. B* **84**, 235126 (2011).
- [77] X.-Q. Sun, B. Lian, and S.-C. Zhang, Double Helix Nodal Line Superconductor, *Phys. Rev. Lett.* **119**, 147001 (2017).
- [78] P.-Y. Chang and C.-H. Yee, Weyl-link semimetals, *Phys. Rev. B* **96**, 081114(R) (2017).
- [79] W. Chen, H.-Z. Lu, and J.-M. Hou, Topological semimetals with a double-helix nodal link, *Phys. Rev. B* **96**, 041102(R) (2017).
- [80] F. N. Únal, A. Eckardt, and R.-J. Slager, Hopf characterization of two-dimensional Floquet topological insulators, *Phys. Rev. Research* **1**, 022003(R) (2019).
- [81] K. Wang, A. Dutt, C. C. Wojcik, and S. Fan, Topological complex-energy braiding of non-Hermitian bands, *Nature (London)* **598**, 59 (2021).
- [82] M. Ezawa, Topological semimetals carrying arbitrary Hopf numbers: Fermi surface topologies of a Hopf link, Solomon's knot, trefoil knot, and other linked nodal varieties, *Phys. Rev. B* **96**, 041202(R) (2017).